東京大学 大学院新領域創成科学研究科
基盤科学研究系物質系専攻

平成29年度

修士論文

Analysis of photocarrier mobility in $BaSnO_3$ thin films
$BaSnO_3$ 薄膜の光キャリア移動度評価

2018年1月22日提出
指導教員 Mikk Lippmaa 准教授

木原 勝也

Contents

Chapter 1

Introduction

1.1 Energy and environment problems

Ever since the industrial revolution in the 18th century, economic development has been dependent on the availability of a large sources that power our daily lives. For the most part, these energy needs have been met by fossil fuels such as petroleum, coal, and natural gas. However, the existing fuel sources are limited and consumption of fossil fuels produces massive amounts of CO_2, which is thought to lead to undesirable global warming and climate change due to the greenhouse effect. To solve these problems at a global scale, a sustainable energy source is necessary.

The largest available energy source is the Sun, which provides earth with sufficient energy for all human needs. The most common technique to utilize solar energy for generating electricity is to use solar cells, which can convert solar energy directly into electric current. However, solar cells do not solve the problems of energy storage and transport, which is relatively simple with fossil fuels. Since sunlight is not always available and the amount of sunlight depends on the geographic position, an energy carrier with small negative environmental impact is necessary. Hydrogen is one possible clean energy carrier because it can be stored and transported relatively easily, while combustion of hydrogen either in an engine or a fuel cell only produces water as a waste product. Solar energy can be used directly to produce hydrogen either in a photocatalytic or a photoelectrochemical water splitting cell. Since the discovery of photoelectrochemical water splitting using a TiO_2 electrode, as reported by Fujishima and Honda in 1972 [1], a large research effort has been made to find efficient materials for splitting water into hydrogen and oxygen. However, efficient materials for practical use have not been found so far. Therefore, it is quite important to study the physical processes that limit the energy conversion efficiency in semiconductor materials and to gain a better understanding of the mechanism of photoelectrochemical water splitting.

1.2 Energy conversion efficiency of photoelectrochemical water splitting

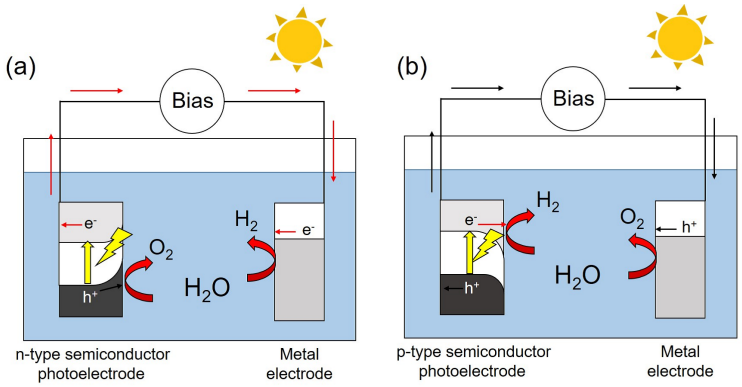

Figure 1.1: Schematic illustration of a photoelectrochemical water splitting cell that uses (a) an n-type semiconductor photoanode and a metal counter electrode, (b) a p-type semiconductor photocathode and a metal counter electrode.

Figs.1.1 (a,b) shows a schematic illustration of a photoelectrochemical water splitting cell using an n-type semiconductor photoelectrode or a p-type semiconductor photoelectrode, respectively. There are three main steps in the water splitting reaction. The first step is the absorption of light. When a semiconductor is irradiated with light for which the photon energy is larger than the semiconductor band gap, photoexcited electrons and holes are generated. The second step is charge separation and drift of photocarriers. Some of the photocarriers migrate to the surface of the electrode due to an internal electric field, while other carriers may be lost to recombination. The diffusion length $L_{\text{diffusion}}$ can be written as

$$L_{\text{diffusion}} = \sqrt{D\tau} = \sqrt{\frac{kT}{q}\mu\tau}, \tag{1.1}$$

where k is the Boltzmann constant, T is the temperature of the semiconductor, q is the charge of a carrier, μ is the mobility of a carrier, and τ is the lifetime of a carrier. This step is strongly affected by sample crystallinity, which determines the density of point defects that act as rapid recombination centers. The final step is the surface chemical reaction. Electrons reduce water to form H_2 on the counter electrode while holes oxidize water to form O_2 on the semiconductor surface. The photoelectrode type, i.e., a photoanode or photocathode depends on the external bias and the semiconductor properties. An n-type semiconductor works as a photoanode that forms a space charge

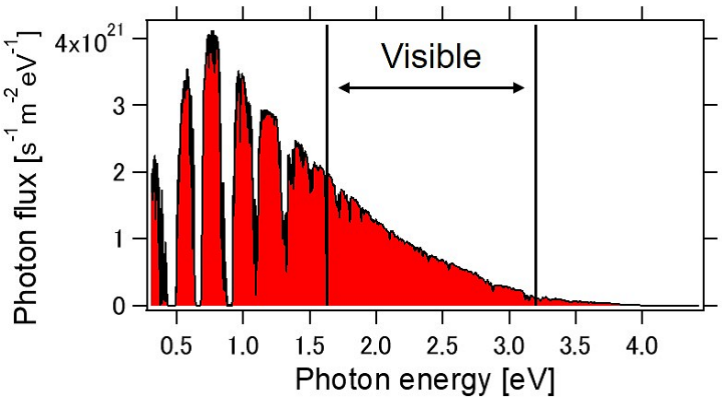

Figure 1.2: The spectrum of the photon flux in sunlight at sea level (AM1.5).

region with upward band bending near the water interface. This promotes the diffusion of holes to the surface, leading to water oxidation and oxygen gas evolution. In case of a *p*-type semiconductor, a downward band bending space charge region forms close to the surface and the material works as a photocathode, where electrons migrate toward the surface and reduce water, evolving hydrogen gas. The energy conversion efficiency of sunlight to chemical stored energy is determined by these three steps.

The efficiency of the first step is mainly determined by the band structure of a material. Since the redox potential of H^+/H_2 and O_2/H_2O are 0 V and 1.23 V vs a reversible hydrogen electrode (RHE), the band gap of the photoelectrode material must be larger than 1.23 eV. For high-efficiency redox reactions to occur, the activation energy for each redox reaction should be considered. The potential barrier of each redox reaction is about 0.5 V. Taking this into consideration, the band gap of the semiconductor material should be close to 2 eV. In addition to the band gap size, the stability of materials during the photoelectrochemical reaction is also important. Some typical semiconductors such as Si, CdS, and GaAs are unstable in electrochemical reactions due to photocorrosion, which is a common reaction in many semiconductors where photo-excited holes react with the semiconductor itself, rather than water, and degrade the semiconductor. For these reasons, oxide semiconductor materials are suitable for photoelectrochemical water splitting, since the band gap can be sufficiently wide and many oxides are relatively stable in water.

For example, TiO_2 and $SrTiO_3$, which are famous photocatalytic materials, have a 3.2 eV band gap and both are stable in water. However the band gaps of these materials are well above the optimal 2 eV value, and too large to absorb sunlight efficiently. Fig.1.2 shows the spectrum of solar photon flux at sea level, calculated for air mass (AM) 1.5. Most of the energy is in the visible region. Materials with wide band gaps like TiO_2 and $SrTiO_3$ cannot utilize most of the suns energy. The usual

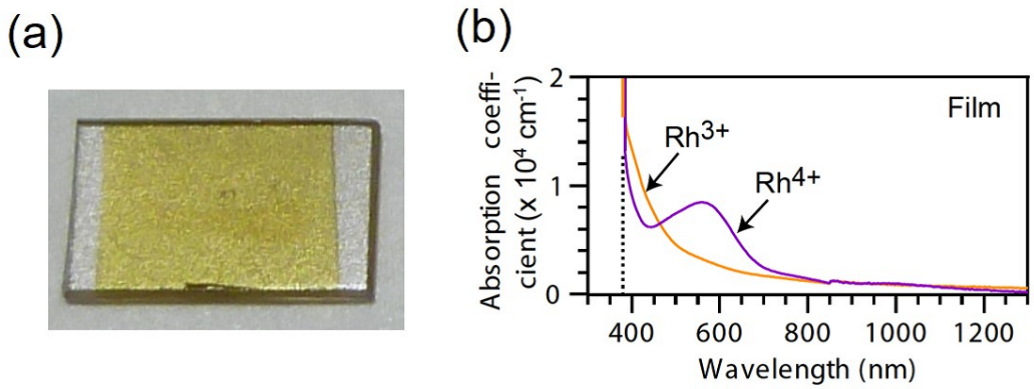

Figure 1.3: (a) Picture of a Rh^{3+}:$SrTiO_3$ thin film sample, (b) the absorption coefficient spectrum of the Rh-doped $SrTiO_3$ thin film. [4]

strategy to solve this problem is to introduce impurity doping into the semiconductor. In the case of $SrTiO_3$, the band gap can be reduced to $\sim$ 2 eV by doping with Rh or Cr [2, 3]. In particular, Rh^{3+}:$SrTiO_3$ shows *p*-type semiconductor behavior in photoelectrochemical measurements, with a large overpotential for hydrogen evolution from water. Figs. 1.3(a,b) show a picture of a Rh^{3+}:$SrTiO_3$ thin film sample and the absorption coefficient spectrum of Rh-doped $SrTiO_3$ [4]. As shown in Fig. 1.3 (a), the Rh^{3+}:$SrTiO_3$ thin film has a yellowish color due to absorption in the visible light region. However, the solar energy conversion efficiency is still low due to the small absorption coefficient in the visible region and a very short diffusion length of photogenerated carriers. Since the diffusion length of photogenerated carriers are determined by drift mobility and lifetime, one strategy to improve the efficiency of photoelectrochemical performance is to use a material with a higher carrier mobility at room temperature. There are two main types of photocatalytic oxide materials as shown Fig. 1.4. Many photocatalytic transition metal oxide materials such as TiO_2, $SrTiO_3$, $KTaO_3$ etc., contain metal ions with a d^0 electronic configuration and their conduction bands are usually composed of *d*-orbitals [5] that tend to exhibit relatively low carrier mobilities at room temperature. On the other hand, the second group of oxides, such as $BaSnO_3$, contain metal ions with a d^{10} electronic configuration and the conduction band is composed of *s*-orbitals [6]. The conduction band thus has large dispersion due to a larger overlap between the *s*-orbitals. Therefore, it can be expected that photoexcited electrons in typical d^{10} metal oxides may show a longer diffusion length at room temperature.

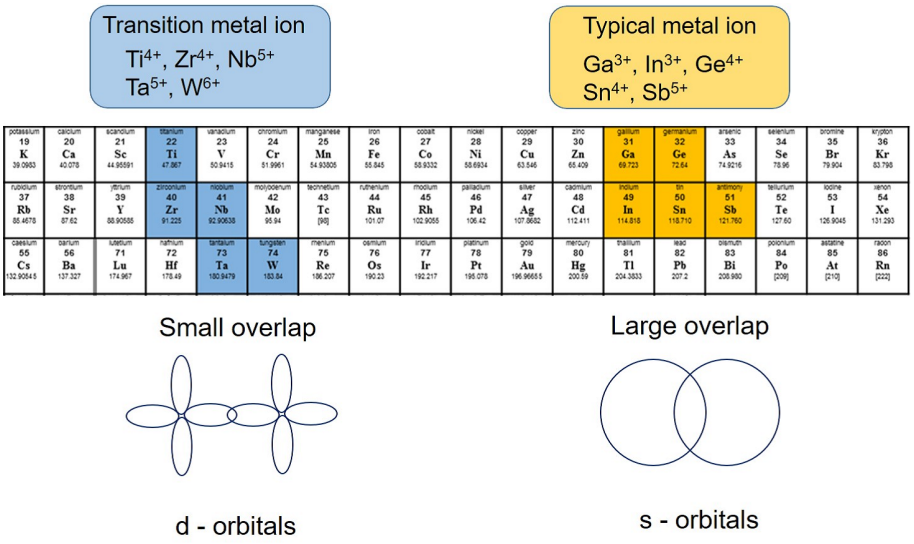

Figure 1.4: Elements that are used in photocatalytic water splitting oxides.

1.3 Aim of this study

Although the drift mobility of photocarriers is an important factor for optimizing the efficiency of photoelectrochemical electrodes, there is very little published data on the drift mobility of various nondoped oxide materials. Therefore, analysis of the drift mobility of photocarriers in typical metal oxide material is a interesting starting point for high-efficiency photocatalytic material development. Since photoelectrochemical electrodes require fairly wide gap semiconductors, the materials are good insulators in dark conditions and thus conventional mobility measurement techniques, such as the Hall effect, cannot be used.

Time-of-flight is a common technique for evaluating transport properties of semiconducting or insulating materials under transient conditions. For this measurement, a high-crystallinity epitaxial thin films or single crystals may be used. Although there are various kinds of typical metal oxides that could potentially be used in photoelectrochemical cells, such as indates (In oxides) [7], gallates (Ga oxides) [8], stannates (Sn oxides) [7], germanates (Ge oxides) [9] and antimonides(Sb oxide) [7], stannates are relatively cheap and abundant materials that may be suitable for mass production and practical use. Among stannates, $BaSnO_3$ is a suitable starting point because there are many papers about $BaSnO_3$ epitaxial thin films and $BaSnO_3$ thin film growth is relatively easy due to the simple crystal structure. In this work, I analyzed the drift mobility of $BaSnO_3$ thin films by the time-of-flight technique and evaluate the photoelectrochemical performance of this material.

1.4 Physical properties of $BaSnO_3$

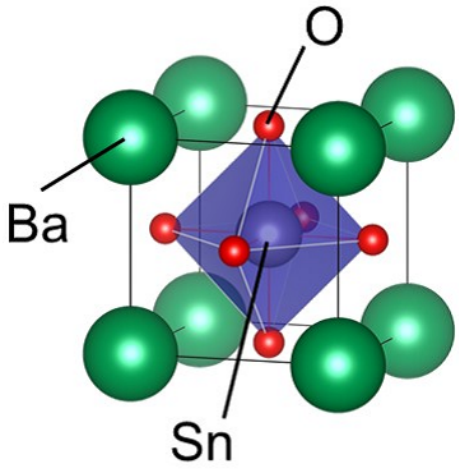

Figure 1.5: The perovskite crystal structure of $BaSnO_3$.

$BaSnO_3$ (BSO) is known to form an ideal cubic perovskite structure with a lattice constant of $a = 4.116$ Å in which the Sn-O-Sn bond angle is close to 180°, as shown in Fig. 1.5. $BaSnO_3$ is a transparent wide-gap semiconductor with an optical gap of more than 3.1 eV [10–12]. The electronic band structure and density of states for $BaSnO_3$ are shown in Fig. 1.6 [13]. The width of the hatching is proportional to the contribution of the particular atomic orbital near the Fermi level to the band structure. $BaSnO_3$ has a highly dispersive conduction band with mainly Sn 5s character while the valence band consists of O 2p orbitals, in common with many other oxides [10, 13]. $BaSnO_3$ is an interesting starting point for developing new types of light absorber materials due to the s character of the conduction band, which can sustain higher carrier mobility than the narrow d-character conduction bands of well-known titanates that were discussed earlier.

Doped derivatives of $BaSnO_3$ have been studied as transparent conducting oxide materials that show high electrical conductivity while remaining transparent in the visible light region. La-doped $BaSnO_3$ single crystals grown by the flux method show very high mobility of 320 cm^2/sV at room temperature [14]. In thin film form, La-doped $BaSnO_3$ samples show somewhat lower mobilities of 26 to 70 cm^2/sV on $SrTiO_3$ substrates and of 150 cm^2/sV on $PrScO_3$ [14–16] due to grain boundaries and dislocations. The high mobility originates from the small effective mass and long relaxation time

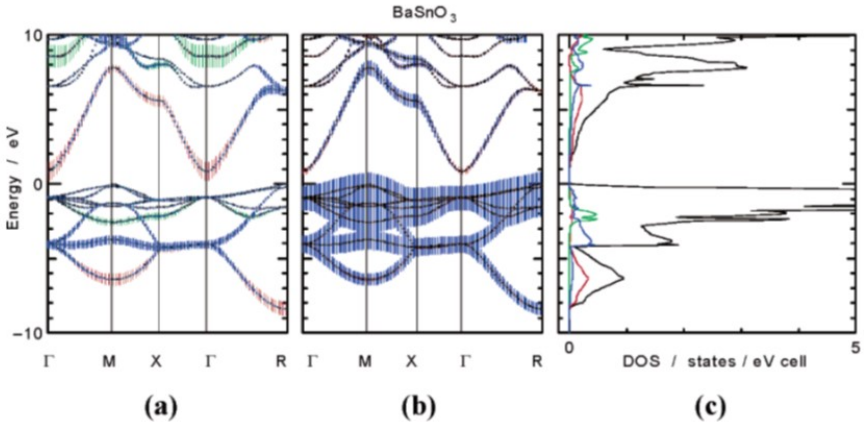

Figure 1.6: The electronic band structure and density of states of $BaSnO_3$. (a) Orbital contribution of Sn $5s$ (red), Sn $5p$ (blue), and Ba $6s$ (green) orbitals to the band structure. (b) The O $2s$ (red) and O $2p$ (blue) contributions to the band structure. (c) The density of states diagram. The Ba $6s$ contribution (green), the Sn $5s$ contribution (red), the Sn $5p$ contribution (blue), and the total electronics DOS (black). [13]

since the mobility can be expressed as

$$\mu = \frac{e\tau}{m^*}, \tag{1.2}$$

where e, τ, and m^* are the electron charge, carrier relaxation time, and the effective mass. There are many paper about the effective mass of $BaSnO_3$ and the effective mass values are reported as 0.06 - 3.7 m_0 depending on evaluation methods [17–19].

Chapter 2

Methods and techniques

The experimental equipment and techniques used in this study are introduced in this Chapter. Thin film samples were fabricated by pulsed laser deposition (PLD). Reflection high-energy electron diffraction (RHEED) was used for in-situ monitoring of the surface morphology and the growth mode during film deposition. X-ray diffraction (XRD) analysis was used for measuring the lattice parameter of the films and for evaluating film crystallinity. The three-dimensional surface profile images of thin films were measured by atomic force microscope (AFM). The film thickness and chemical composition of $BaSnO_3$ thin films were analyzed by x-ray fluorescence (XRF). The drift mobility of $BaSnO_3$ thin films were analyzed by time-of-flight (TOF) technique. The cyclic voltammetry curves of $BaSnO_3$ samples were measured to evaluate photoelectrochemical performance.

2.1 Pulsed laser deposition (PLD)

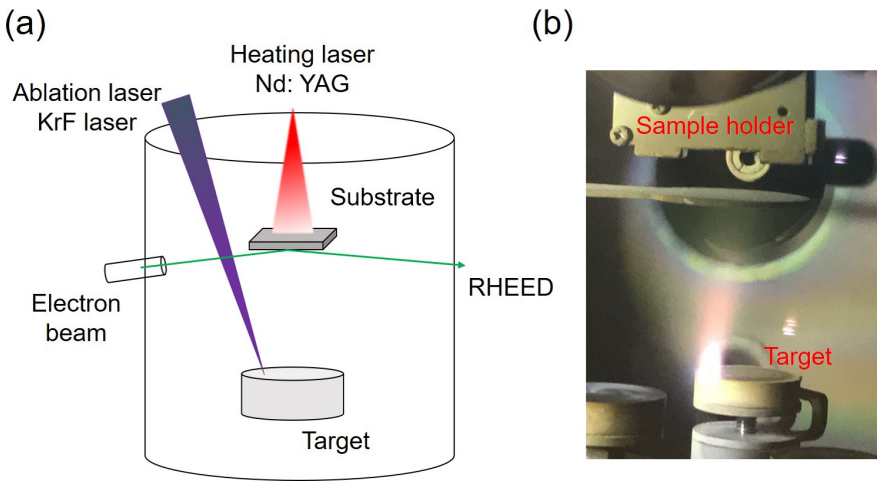

Figure 2.1: (a) Schematic image of a PLD system, (b) Inside view of the PLD chamber showing the plume formed during target ablation.

There are several techniques that can be used for growing complex oxide thin films that have good crystallinity and also provide atomic-level control over the growth rate and film thickness. Pulsed laser deposition is one such technique that allows us to grow thin films of most complex oxides over a wide range of process parameters such as temperature and ambient gas pressure. Fig. 2.1 (a) shows a schematic image of a PLD system. The ablation plume captured during target ablation can be seen in Fig. 2.1 (b). In PLD, a high-power pulsed laser beam is focused on the surface of a ceramic target in a vacuum chamber. The target material is vaporized, forming a plasma plume that carries material from the target to the substrate, where the plasma condenses, forming a crystalline film. The adatoms brought to the film surface by the deposition plume can subsequently diffuse on the film surface until they encounter other adatoms and form new clusters on flat terraces or attach to existing clusters or step edges. There are three conventional modes of film nucleation and growth. If the adatom flux to the surface is constant in time, the stability of a particular growth mode depends on thermodynamic parameters, such the film surface energy and the interface energy between the film and the substrate. Fig. 2.2 illustrates these growth modes: (a) layer-by-layer growth (Frank-van der Merwe mode), (b) island growth (Volmer-Weber mode), (c) wetting layer and island growth (Stranski-Krastanov mode). When the interaction between the substrate and the film is strong enough, and the lattice mismatch is less than about 4%, layer-by-layer mode is possible [20]. In an ideal layer-by-layer growth mode, a single unit cell layer is completely filled before the next layer starts to grow Fig. 2.2(a).

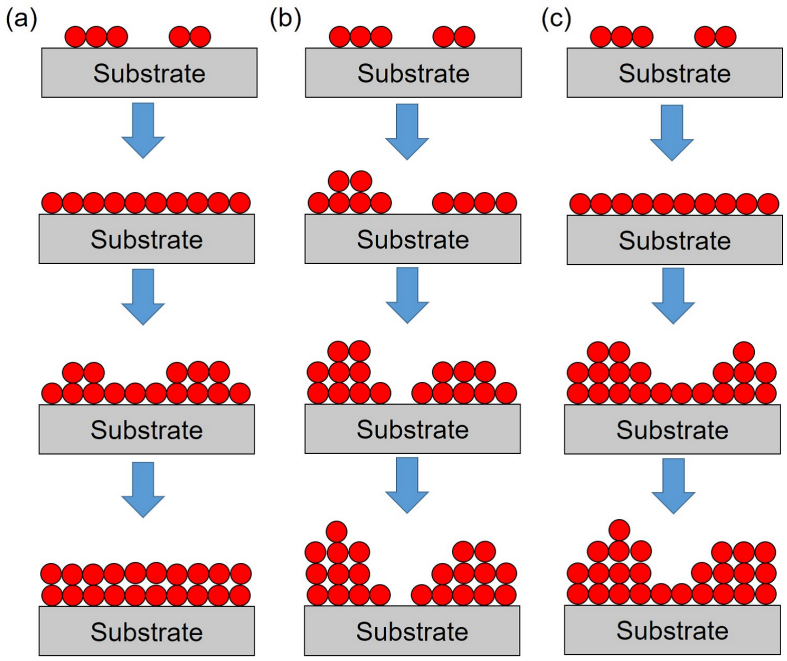

Figure 2.2: Schematic illustration of the three film growth modes.

On the other hand, three-dimensional nucleation of islands occurs when the interface energy of the film is high and the lattice mismatch between the film and the substrate is large (Fig. 2.2(b)). These islands grow until they coalesce and form a continuous film. This type of growth may lead to the formation of gran boundaries. Wetting layer and island growth is a mixture of Figs. 2.2(a) and 2.2(a)(b). A few first layers grow in the layer-by-layer mode, but three-dimensional island growth starts after an the initial wetting layer has formed. This conversion of growth modes can be explained by the increasing stress with increasing layer thickness due to lattice mismatch. The composition and crystallinity of the thin films can be controlled by adjusting the deposition conditions such as the growth temperature, ambient gas pressure, and the ablation laser fluence. The background oxygen pressure is an important process parameter in oxide film growth, which can affect the formation of the desired phase, cation valence, film stoichiometry, and crystallinity. The PLD system uses dynamic pressure control by constantly feeding fresh oxygen into the chamber with a variable leak valve, while the chamber is evacuated by two turbomolecular pumps backed by conventional rotary pumps. The process pressure can be set anywhere between the base pressure of about 10^{-8} Torr and the maximum ambient pressure of about 1 Torr where PLD plume formation is still possible. The pressure adjustment is achieved by adjusting the pumping rate with gate and angle valves while the gas inlet rate is adjusted with a molecular

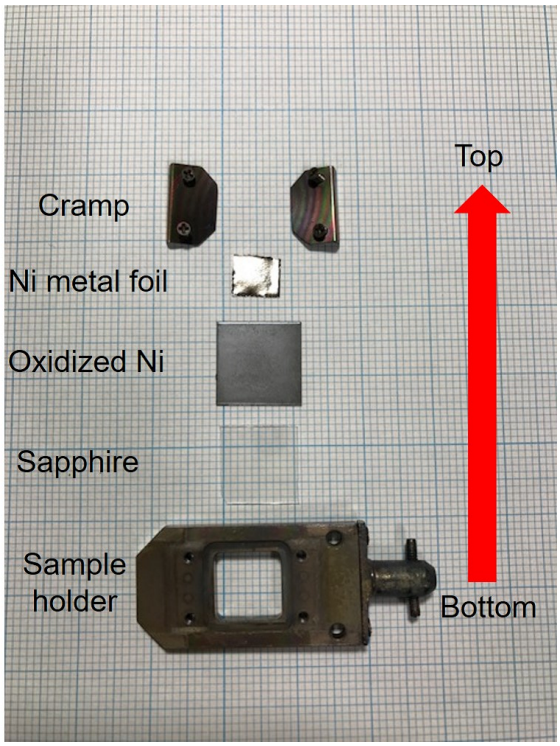

Figure 2.3: Components of a high-temperature sample holder.

leak valve. Single crystal substrates were mounted on sample holders and loaded into a sample stage in the vacuum chamber. Fig. 2.3 shows the structure of the sample holder that was used for $BaSnO_3$ film growth. Most oxide thin films need to be grown at high temperature to obtain good crystallinity. For this purpose, the substrates were heated with a Nd:YAG laser operating at the fundamental 1060 nm wavelength. To absorb this laser light, an oxidized Ni (200 μm thick) sheet was used as a light absorber and heat spreader. Another Ni metal foil (5 μm thick) was inserted between the substrate crystal and the oxidized Ni sheet to obtain uniform heat contact. The high-temperature parts of the sample holder were supported by a sapphire sheet that also decreases heat loss. A Krypton Fluoride (KrF) excimer laser (Lambda Physik COMPex 201) was used for target ablation with its 248 nm wavelength and 20 ns pulse width. The laser energy density was adjusted by a single focus lens and quartz attenuators.

2.1.1 Reflection high-energy electron difraction (RHEED)

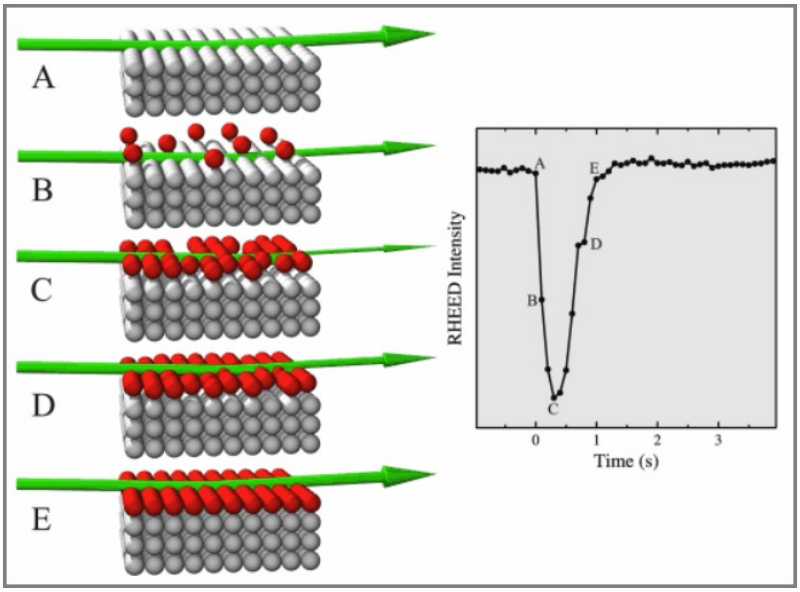

Figure 2.4: Crystal surface models and reflected electron beam intensity variation for layer-by-layer growth. [21]

One of the more difficult problems in complex oxide thin film growth is the control of the crystal surface morphology and the deposition rate, which may be affected by even minor changes in the deposition conditions. Due to that, it is quite useful for thin film growth to monitor the sample surface characteristics during the growth process. In this work, reflection high-energy electron diffraction (RHEED) was used for in-situ monitoring of the surface morphology and the growth rate during film deposition by PLD. RHEED is a surface diffraction technique that is widely used for surface analysis of crystalline materials. RHEED works by firing a narrow electron beam at a sample surface at grazing incidence. Considering the layout of the PLD chamber (Fig. 2.1 (a)), it is easy to see that RHEED measurements do not interfere with the deposition plume. The incidence angle is usually 1 to 2 degrees from the sample surface. The electron beam energy was 25 keV and the beam current was 50 μA. For in-situ monitoring, the reflected and diffracted beams were observed on a phosphor screen with an analog video camera. The surface morphology can be determined from static diffraction patterns. The growth rate can be estimated by monitoring oscillations of the reflected specular beam intensity. Fig. 2.4 shows surface models and reflected beam intensity variations during homoepitaxial layer-by-layer growth of a single unit cell layer of $SrTiO_3$. Before film growth, the surface is atomically flat, which gives a high reflected

beam intensity (Fig. 2.4(A)). When the film deposition starts, the reflection intensity decreases rapidly as adatoms stick to the surface and islands are nucleated. The intensity drop is associated with electron scattering from step edges (Fig. 2.4(B)). At point C (Fig. 2.4), the surface roughness has reached a maximum, which corresponds to a minimum in the specular reflection intensity. As the deposition continues, the reflection intensity starts to increase until all the surface is covered by a complete unit cell layer (Figs. 2.4(C,D,E)). This oscillation process repeats for each unit cell that is grown as long as the layer-by-layer growth mode is maintained.

2.2 X-ray diffraction (XRD)

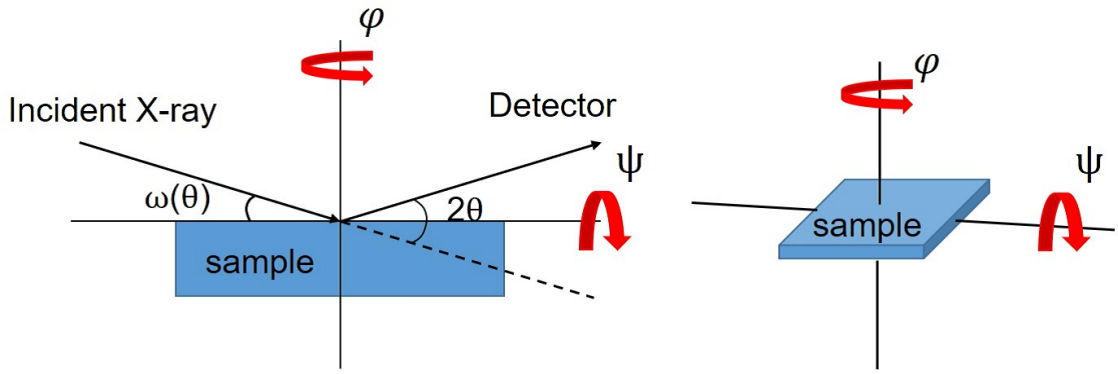

Figure 2.5: Schematic illustration of the sample position and rotation axes for XRD measurement.

X-ray diffraction (XRD) is the most common tool used for analyzing crystal structures. This technique is based on observing the intensity of diffracted x-rays hitting a sample as a function of incident and diffraction angles. Diffraction peaks can be observed when the incident and detection angles satisfy Bragg's Law:

$$n\lambda = 2d \sin\theta, \tag{2.1}$$

where n is an integer describing the diffraction order, λ is the wavelength of the X-rays, d is the lattice spacing, and θ is the diffraction angle from the surface. In this study, XRD was used for characterizing the crystallinity and measuring the lattice parameter of thin films grown by PLD. The crystallinity, orientation, lattice parameter, and the other phases can be analyzed by XRD. A 4-circle diffractometer (Xpert-MRD: Philips) was used for the measurements with a CuKα X-ray source. The wavelength of this characteristic X-ray is 1.5405929 Å. Fig. 2.5 shows a schematic illustration of the sample position and rotation axes (θ, ω, ϕ, ψ) for XRD measurement. For all samples, $2\theta/\omega$ and rocking curve measurements were conducted. In $2\theta/\omega$ measurement, both the incident angle ω and the detector angle 2θ are scanned, while the ratio of $\frac{2\theta}{\omega} = 2$ is maintained. The c-axis lattice spacing of the film can be evaluated by this $2\theta/\omega$ measurement. The c-axis lattice spacing is affected by strain caused by lattice mismatch between the substrate and film materials, stoichiometry changes, and impurities. In a rocking curve measurement, only the incident angle ω is scanned in the vicinity of Bragg angle, while the detector angle is fixed to the position of a Bragg peak. Fig.2.6 shows the schematic illustration of rocking curve. The diffraction condition can be

written in the following using reciprocal lattice vector $\boldsymbol{G}$ and scattering vector $\Delta\boldsymbol{k}$:

$$\Delta\boldsymbol{k} = \boldsymbol{k}' - \boldsymbol{k} = \boldsymbol{G} \tag{2.2}$$

where $\boldsymbol{k}'$ and $\boldsymbol{k}$ are wavevector of the diffracted beam and incident beam. When the incident angle is slightly changed, the scattering vector is also tilted in the radial direction. If the dispersion of the crystal orientation is wide, the Bragg peak become broad in the radial direction. Thus the crystallinity of film can be evaluated by measuring the full width at half maximum (FWHM) of the diffraction peak.

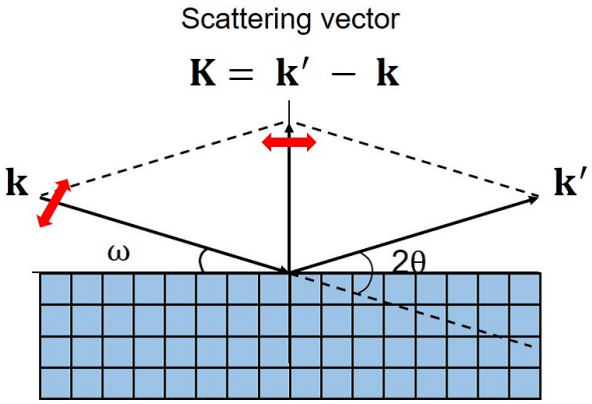

Figure 2.6: Schematic illustration of rocking curve measurement.

2.3 Atomic force microscope (AFM)

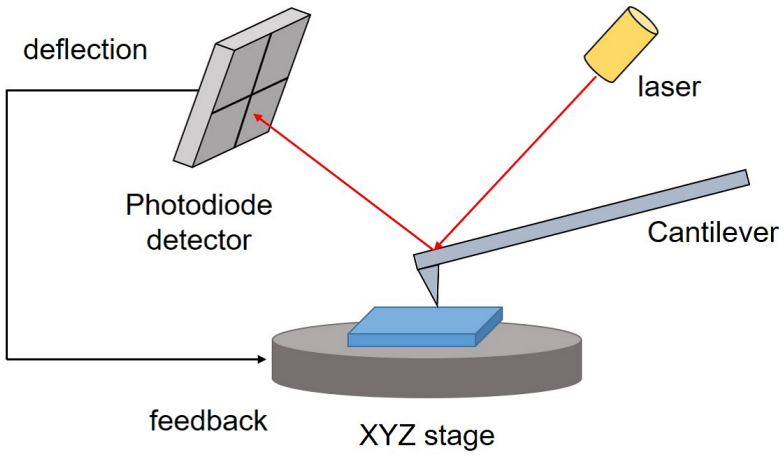

Figure 2.7: Schematic illustration of the AFM system.

Atomic Force Microscopy (AFM) is a type of scanning probe microscopy, which provides a very high resolution three-dimensional surface profile image. The vertical resolution is on the order of a fraction of a nanometer while the spatial resolution is determined by the sharpness of the probe needle. In the measurements discussed here, the lateral resolution was on the order of 10 to 20 nm. There are two basic modes of operation, namely contact mode and non-contact mode, depending on whether the cantilever vibrates during above the surface during measurement or is brought into contact with the surface. The AFM system measures the surface profile by sensing the contact force from the bending of the cantilever in contact mode and from the resonant frequency change of the cantilever in non-contact mode. In this study, the surface morphologies were measured by contact or non-contact mode with a Shimadzu SPM-9600 microscope. The scan areas were usually 1 μm $\times$ 1 μm and 5 μm $\times$ 5 μm. Fig. 2.7 shows a schematic illustration of the AFM system. This system includes a sharp needle attached to a flexible cantilever, a laser diode, a photodetector, and an XYZ sample stage. A laser beam reflects from the back of the cantilever and the reflected light from the cantilever is detected with a multisegment photodiode detector, which measure the deflection of the laser beam from the center (straight cantilever) position. When the needle scans the sample surface, the sample height is adjusted by a piezoelectric actuator included in the XYZ stage so that the deflection is kept constant in contact mode or close to zero in non-contact mode. The deflection of the laser beam corresponds to the bending of the cantilever, which depends on the contact force. From this bending of the cantilever, the AFM system can measure the surface profile in contact mode. On the

other hand, in non-contact mode, a silicon cantilever probe is connected to a resonator. The cantilever is oscillating at the resonant frequency during measurement. When the needle scans the sample surface, the resonant frequency of the cantilever is changed by the atomic-scale force close to the surface. A feedback system in the microscope adjusts the sample height with a piezoelectric actuator so that the resonant frequency is kept constant. From this change of the sample height, the AFM system can measure the surface profile in non-contact mode.

2.4 X-ray Fluorescence (XRF)

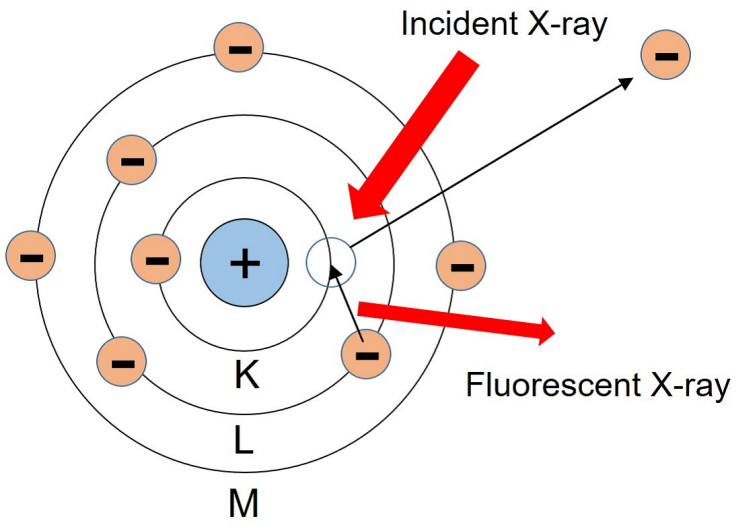

Figure 2.8: Schematic illustration of the principle of the emission of characteristic fluorescent x-rays.

X-ray fluorescence spectroscopy (XRF) is a technique that is widely used for element and chemical composition analysis. This technique detects the characteristic fluorescent X-rays from a material that has been excited by irradiation with high-energy x-rays. Fig. 2.8 shows a schematic illustration of the principle of the emission of characteristic fluorescent X-rays. When a sample is irradiated with x-rays with sufficient energy to excite electrons in inner orbitals, electrons are ejected from the inner orbitals, leaving core holes. When electrons in outer orbitals fill the core-level holes, the excess energy is emitted in the form of photons, where the photon energy is equal to the energy difference of the two orbitals. This energy difference between core-level orbitals is unique for each element, which means that constituent elements in a material can be determined by measuring the fluorescence x-ray emission spectra. In this study, x-ray fluorescence was analyzed by wavelength dispersive x-ray fluorescence (WDXRF) spectrometer (Rigaku Primus IV). Fig. 2.9 shows a schematic illustration of the Rigaku WDXRF system. In this system, the different energies of the characteristic x-rays emitted from a sample are diffracted into different directions by analyzing crystals. By placing a detector at a certain angle, the intensity of x-rays at a certain wavelength can be measured. The film thickness of a sample also can be estimated from the intensity of x-rays besides the chemical composition. The advantages of the WDXRF system

are high resolution and minimal spectral overlap compared to energy dispersive X-ray fluorescence (EDXRF) in which an energy dispersive detector is used to collect the characteristic x-rays emitted from a sample.

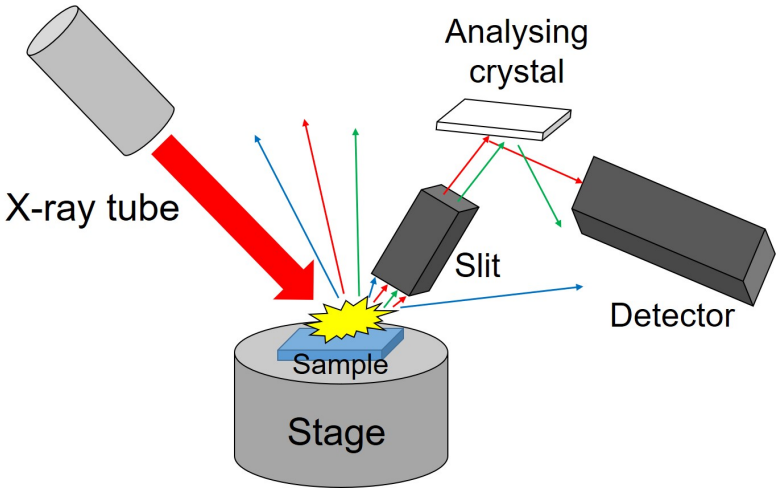

Figure 2.9: Schematic illustration of the WDXRF system

2.5 Optical absorption rate measurement

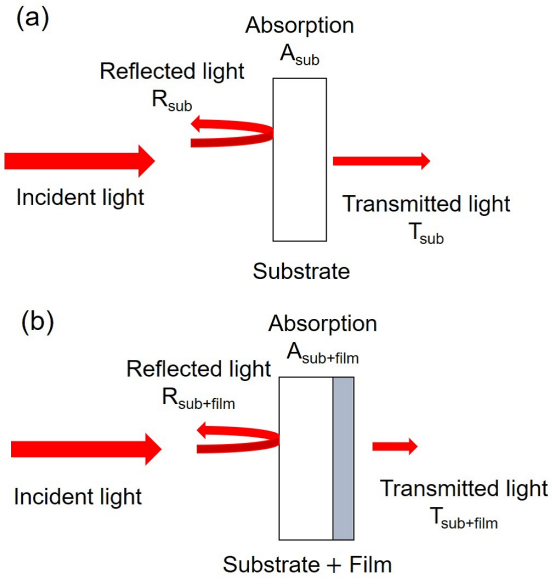

Figure 2.10: Schematic illustration of the transmittance measurement.

The optical absorption coefficient α of a material tells us how far into the material light of a particular wavelength can penetrate. The absorption coefficient can be expressed as

$$\alpha = -\frac{1}{x}\ln(\frac{I}{I_0}), \tag{2.3}$$

where α is the absorption coefficient, I_0 is the incident light intensity at $x = 0$, and I is the light intensity at depth x. When reflection from the surface is negligible, this equation can be written using transmittance T and sample thickness d in the following form,

$$\alpha = -\frac{1}{x}\ln(\frac{I}{I_0}) = -\frac{1}{d}\ln(T). \tag{2.4}$$

In this study, the transmittance spectra of $BaSnO_3$ thin films were measured to calculate the absorption spectra with a Jasco V570 UV-Vis-NIR spectrophotometer in the wavelength range of 190 to 1500 nm. The instrument selects a suitable light source automatically, switching from a deuterium lamp for the ultraviolet (UV) range (190 - 350 nm) to a halogen lamp for the visible and infrared (IR) range (340 - 1500 nm). To minimize the contribution of the substrate, double-side-polished MgO substrates were used. This substrate material has a wider optical band gap than $BaSnO_3$. At first, the

transmittance spectrum of the substrate (T_{sub}) was measured (Fig. 2.10(a)). The transmittance spectrum of a thin film on the same substrate material ($T_{sub+film}$) was then measured (Fig. 2.10(b)). Assuming that the reflectance of the film is negligible, the transmittance spectra and the absorption coefficient of the film were calculated using the following equations

$$T_{film} = \frac{T_{sub+film}}{T_{sub}}, \tag{2.5}$$

$$\alpha = -\frac{1}{d}\ln(T_{film}). \tag{2.6}$$

2.6 Time-of-flight (TOF) measurement

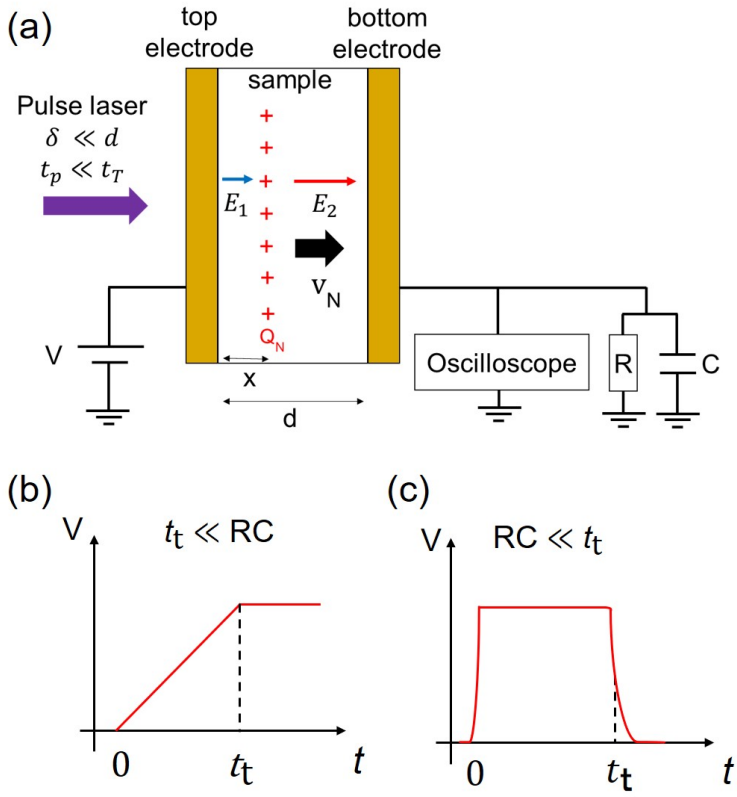

Figure 2.11: (a) Schematic illustration of the TOF measurement, typical signal shape obtained by TOF measurements. (b) Charge integration method (c) Current duration method.

The time-of-flight (TOF) technique is a very direct approach to evaluating transport properties of a semiconducting or insulating material. This technique is particularly suitable for low carrier mobility materials where Hall effect measurement is impossible, as discussed in a number of studies [22–26]. The principle of this technique has been reviewed by Spear [27], together with problems caused by trapping and space charge effects. In this method, the drift mobility of carriers can be evaluated by measuring the transit time of drifting nonequilibrium carriers. In the following, the principle of this method is introduced briefly.

Fig. 2.11 (a) shows a schematic illustration of the TOF measurement setup. To simplify the argument, consider a trap-free insulating solid sample with top and bottom metallic electrodes. The top electrode should be semi-transparent for optical photo-

excitation of carriers. A bias source is connected to the top electrode and the bottom electrode is returned to ground potential through a resistor which is much smaller than the sample resistance. The C in Fig. 2.11 (a) denotes the total capacitance across all circuits, including the input of the oscilloscope. The potential generated by a current flowing through the resistor R is measured with an oscilloscope. When free carriers are generated by photo-excitation through the semi-transparent top electrode, the excited carriers drifted towards the bottom electrode in an electric field generated by the applied bias V_A. If the excitation light pulse (t_e) is considerably shorter than the transit time of the generated carriers across the sample and the penetration depth of the excitation light (δ) is much shorter than the sample thickness d, the drifting narrow sheet of carriers at x modifies the applied electric field $E_A = \frac{V_A}{d}$ in the sample:

$$E_1(x) = E_A - \frac{Ne}{\epsilon A}(1 - \frac{x}{d}), \tag{2.7}$$

$$E_2(x) = E_A + \frac{Ne}{\epsilon A}\frac{x}{d}, \tag{2.8}$$

where N is moving carrier number, e is charge of carrier, A is a electrode area ϵ is the dielectric constant of solid. It should be noted that this description can be applied only to an insulating solid in which the dielectric relaxation time is much longer than the transit time. The situation is completely different from the drift mobility of minority carriers in a doped semiconductor such as Ge [28], Si [29], GaAs [30] where the condition of the local space charge neutrality during carrier transit is always satisfied and thus the drifting carrier doesn't modify the applied electric field.

There are two ways to determine the transit time of the drifting carriers, depending on the time constant of the readout circuit, RC. The choice between the two methods depends on the order of magnitude of t_t and the sample capacitance. The first method relies on charge integration and in this method the RC value must be much larger than the transit time t_t. As the drifting carriers modify the applied electric field, the changing electric field causes a displacement charge to be generated in the bottom electrode. The amount of change of the charge for the bottom electrode is given by

$$\Delta q = \frac{Nex}{d}. \tag{2.9}$$

The potential measured across the resistor R is

$$\Delta V(t) = \frac{Ne}{Cd}vt \quad (0 < t < t_t), \tag{2.10}$$

$$\Delta V(t) = \frac{Ne}{C} \quad (t_t < t << RC), \tag{2.11}$$

where $v = d/t_t$ is the drift velocity. The typical signal obtained in this method is shown in Fig. 2.11(b). The transit time of the drifting carriers can be measured from the time

of the linear rising edge. Alternately, t_t can be measured from the duration of the current pulse induced by the drifting carriers. In this second method, the time constant RC must be much shorter than t_t. The displacement current across the resistance R induced by drifting carrier is

$$i = \frac{Ne}{d}v. \tag{2.12}$$

Therefore, The induced voltage is

$$\Delta V(t) = R\frac{Ne}{d}v \quad (0 < t < t_t), \tag{2.13}$$

$$\Delta V(t) = 0 \quad (t_t < t). \tag{2.14}$$

A typical signal obtained by this method is shown in Fig. 2.11(c). The drift mobility of carriers can be calculated by following equation:

$$\mu = \frac{d}{E_A t_t} = \frac{d^2}{V_A t_t}. \tag{2.15}$$

In this study, thin film samples were prepared on Nb0.5wt% doped $SrTiO_3$ substrate by PLD. The 0.5wt% Nb-doped $SrTiO_3$ substrates have sufficiently low resistivity to be used as bottom electrodes. Semitransparent top electrodes were deposited by vacuum vapor deposition. For free carrier excitation, a frequency-quadrupled Nd:YAG laser (Autex PNU-M01210) was used at a wavelength 266 nm with a 350 ps pulse width. The voltage generated on the resistance placed in series with the sample was measured as a function of time with a 500 MHz storage oscilloscope (Tektronix TDS3054B).

2.7 Photoelectrochemical measurement

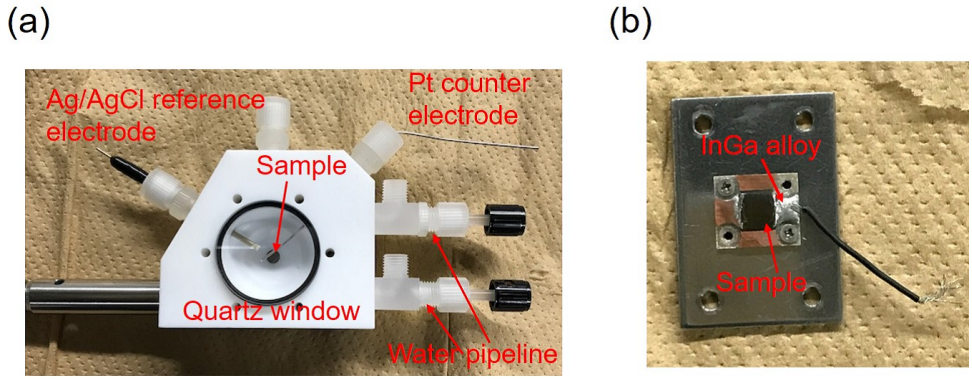

Figure 2.12: (a) The electrochemical cell used for cyclic voltammetry, (b) sample holder for the electrochemical cell

$BaSnO_3/Sr_2RuO_4/SrTiO_3$ heterostructure samples were prepared for photoelectrochemical measurement. Sr_2RuO_4 films were used as bottom electrode. The photoelectrochemical performance of $BaSnO_3$ samples were analyzed in a standard three-electrode configuration with potentiostat (Bio-Logic Science Instruments, SP-150). The cyclic voltammetry curves were measured under UV light illumination with 100W Xe lamp (Asahi spectra, LAX101) and band-pass filter, Pt counter electrode and a Ag/AgCl reference electrode in a 0.1 M K_2SO_4 aqueous solution. Before the each measurement, The aqueous solution were bubbled with nitrogen gas for more than 30 minutes to remove dissolved oxygen. The electrochemical cell is shown Fig. 2.12 (a) The $BaSnO_3$ samples were put on the electrochemical cell with a sample holder shown in Fig. 2.12 (b). An InGa alloy was used to make electric contact between bottom electrode of sample and the potentiostat. The aqueous solution was flowed into the cell through the water pipeline and UV light was illuminated through a quartz window.

The incident photon to current efficiency (IPCE) of $BaSnO_3$ sample was evaluated with the monochromator (Bunkoukeiki, BML-10J). IPCE can be written in the following:

$$\begin{aligned} IPCE(\%) &= \frac{\text{Number of photocarrier used for electrochemicalreaction } [1/\text{cm}^2]}{\text{Incident photon flux } [1/\text{cm}^2]} \times 100 \\ &= \frac{hc}{e\lambda} \frac{\text{Photocurrent density } [\text{A}/\text{cm}^2]}{\text{Light intenisty } [\text{W}/\text{cm}^2]} \times 100 \end{aligned} \tag{2.16}$$

where h, c, e and λ are the Planck constant, the speed of light, the elementary charge and the wavelength of illuminated light. The power of illuminated light was measured

with power meter (THORLABS, S120VC) taking the effect of the quartz window and aqueous solution into consideration.

Chapter 3

Drift mobility measurement for $BaSnO_3$ thin films

The experimental results are discussed in this Chapter. The work can be divided into four stages, starting with the optimization of thin film growth conditions to obtain $BaSnO_3$ films with the best crystallinity. The absorption spectra of the $BaSnO_3$ films were calculated from transmittance spectra to determine the band gap of the films. The drift mobilities of $BaSnO_3$ films were estimated from several types of carrier injection experiments. Finally, the photoelectrochemical response of the films is discussed.

3.1 Optimization of growth conditions for $BaSnO_3$ thin films

3.1.1 Substrate for $BaSnO_3$ thin films

The matching of lattice parameters and crystal structures between a thin film and a substrate is quite important for high-quality epitaxial thin film growth. In the case of $BaSnO_3$ thin film growth, $BaSnO_3$ single crystal substrates are not commercially available. Although there are several paper about $BaSnO_3$ single crystal growth [14,31], the maximum size of single crystals is on a mm scale and the growth procedures are complicated. For this reason, $BaSnO_3$ thin films are usually grown on other substrate materials such as $SrTiO_3$ [14, 15], MgO [32], or $PrScO_3$ [16]. Table 3.1 shows the crystal structure, lattice parameter, lattice mismatch, and optical gap of $BaSnO_3$, $SrTiO_3$ (STO), MgO and $(LaAlO_3)_{0.3}(SrAl_{0.5}Ta_{0.5}O_3)_{0.7}$ (LSAT). [33–36]

$BaSnO_3$ films were grown on these substrates at 850°C at an oxygen background pressure of 10 mTorr. Fig. 3.1(a) shows several representative XRD $2\theta - \omega$ scan of $BaSnO_3$ thin film samples grown on $SrTiO_3$, MgO, and LSAT substrates in the range of 5° to 120°. Only (00l) family of peaks were observed in these patterns, which is

Table 3.1: $BaSnO_3$ and substrate materials

sample	structure	lattice parameter (mismatch)	optical gap (eV)
$BaSnO_3$	cubic perovskite	4.116 Å	3.4
$SrTiO_3$	cubic perovskite	3.905 Å (5.4%)	3.2
LSAT	cubic perovskite	3.87 Å (6.4%)	3.6
MgO	rock salt	4.21 Å (2.2%)	4.6

consistent epitaxial growth of films on all three types of substrate. Figs. 3.1(b,c) shows narrow angle scans around the (002) peaks for these films and the corresponding rocking curves of the $BaSnO_3$ film (002) peaks. The black line at 43.9603° in Fig. 3.1(b) shows the expected (002) peak position of bulk $BaSnO_3$ [33]. The diffraction peak positions of the films are slightly shifted from the bulk position due to lattice strain and possibly due to stoichiometry changes in films. Secondary phase peaks were observed at 45.1° in the XRD patterns of films grown on $SrTiO_3$ and LSAT substrates. The origin of these peaks is discussed in Section 3.1.2. The FWHM of the rocking curve of the film grown on $SrTiO_3$ is an order of magnitude narrower than others. It means that the crystallinity of this film is much better than for the other films. Fig. 3.1(d) shows AFM images of the three types of samples grown on different substrates. The grain structure is clearly visible for all films although the average grain size and shape are different due to varying lattice mismatch between the film and the substrate. The roughness of the film surface on $SrTiO_3$ and LSAT is smaller than for the film grown on MgO. From the rocking curve and AFM measurement results, I conclude that $SrTiO_3$ is a suitable substrate material for the growth of $BaSnO_3$ films with good crystallinity.

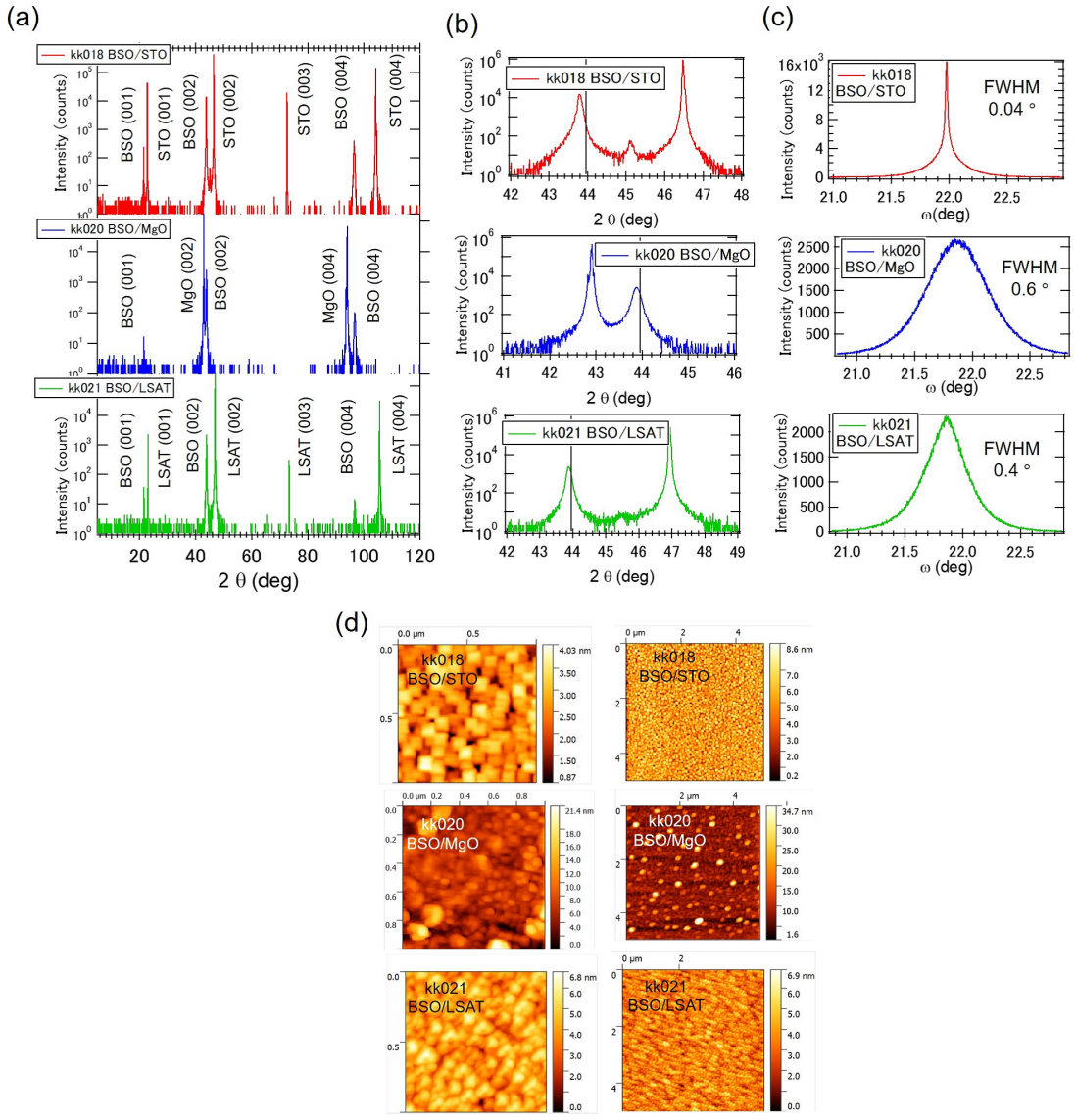

Figure 3.1: XRD patterns for $BaSnO_3$ films grown on $SrTiO_3$, MgO, and LSAT substrates: (a) wide scan, (b) narrow scan around (002) peaks, and (c) rocking curves of the $BaSnO_3$ (002) peaks, (d) AFM images of $BaSnO_3$ films grown on $SrTiO_3$, MgO, and LSAT substrates.

3.1.2 Growth condition of $BaSnO_3$ thin films on $SrTiO_3$ substrates

A difficult problem with $BaSnO_3$ thin film growth is SnO and Sn volatility. There have been several studies the looked into preventing Sn evaporation from $BaSnO_3$ thin films, such as using higher oxygen background pressure during growth [14], solid phase epitaxy [15], and source material modifications [16]. Typical reported PLD growth conditions for $BaSnO_3$ films are 700 to 900°C growth temperature and 50 to 100 mTorr oxygen pressure [14, 15, 17, 37]. Fig. 3.2 shows the effect of changing the growth temperature at a constant background pressure of 100 mTorr on the XRD patterns close to the $BaSnO_3$ (002) peaks. The base of the (002) peaks of films grown at 950°C and 1150°C is broader than for the sample grown at 750°C. There are several peaks components visible in the XRD pattern of the 1150°C film. These additional peaks are most probably caused by a film stoichiometry change and phase segregation due to Sn loss. The optimal growth temperature for $BaSnO_3$ films appears to be around 750°C.

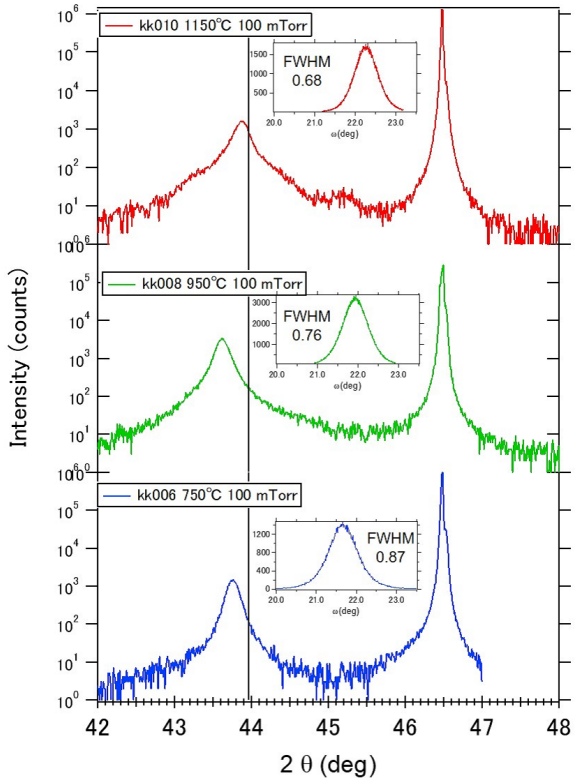

Figure 3.2: Effect of growth temperature on the XRD patterns close to the (002) peak position of $BaSnO_3$ for films grown at 100 mTorr.

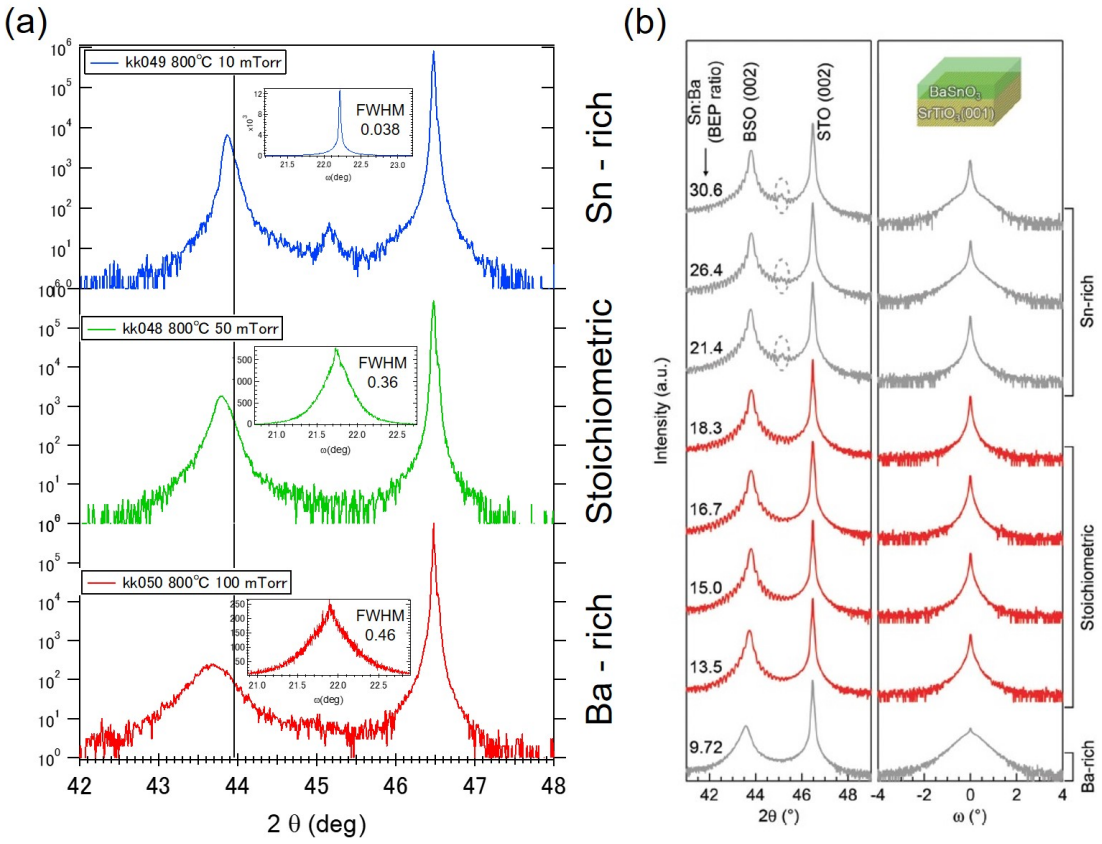

Figure 3.3: (a)The effect of the oxygen pressure on the XRD patterns in the vicinity of the $BaSnO_3$ (002) peak for film grown at 800°C, (b) Reference XRD patterns of $BaSnO_3$ films grown on $SrTiO_3$ substrates by MBE with different Sn : Ba. [39]

Fig. 3.3 (a) shows the oxygen pressure effect on the XRD patterns of the (002) peaks of $BaSnO_3$ film grown at 800°C. The insets of XRD patterns show the rocking curve profiles of the $BaSnO_3$ (002) peaks. The FWHM of the rocking curve for the 10 mTorr film is an order of magnitude narrower than for the other samples, which means that the crystallinity of the film grown at 10 mTorr is much better than other films. However, there is a secondary phase peak at around 45.1°. Other groups have also observed this peak in $BaSnO_3$ films grown on $SrTiO_3$ substrates by PLD and MBE [38, 39]. Fig. 3.3 (b) shows reference XRD patterns of $BaSnO_3$ films grown on $SrTiO_3$ substrates by MBE with different Sn : Ba ratios [39]. The secondary phase peaks were observed for films grown in the Sn-rich regime. Table 3.2 shows the XRF result for the BSO films grown at different oxygen pressures. The SnO_2 ratio increases as the oxygen pressure decreases, which is consistent with the appearance of the extra peak in the

Table 3.2: XRF results for $BaSnO_3$ films grown at different oxygen pressures.

Sample	Oxygen pressure	BaO (mol%)	SnO_2 (mol%)
kk049	10 mTorr	49.115	50.885
kk048	50 mTorr	49.914	50.086
kk050	100 mTorr	50.906	49.094

XRD pattern of a film grown at 10 mTorr. The nearly stoichiometric film grown at 50 mTorr and the Ba-rich sample grown at 100 mTorr do not show this peak. This behavior is the same for the MBE-grown films illustrated in 3.3 (b). Table 3.3 shows the XRD peak positions of candidate materials consisting of Ba, Sn, and O that may have diffraction peaks close to the 45° angle [40–43]. Although no other peaks of Sn_2O_3 could be observed, this secondary phase peak is the most probable, since excess Sn is likely to lead to the segregation of the Sn_2O_3 phase. From these results, I conclude that the optimal conditions for $BaSnO_3$ film growth is at 750 to 800°C and 10 to 50 mTorr oxygen pressure. An indication of a Sn-rich film is the appearance of the secondary phase peak which most probably comes from Sn_2O_3. Accordingly, the laser fluence should be adjusted so as to set the composition of the film close to the stoichiometric Ba/Sn ratio at these growth temperatures and pressures.

Table 3.3: X-ray diffraction peak positions of materials consisting of Ba, Sn, and O around the 45° diffraction angle. [40–43]

sample	structure	h k l	peak position
Sn	Tetragonal	2 1 1	44.9021 °
Sn_2O_3	Triclinic	-1 3 1	45.1619 °
$Ba_3Sn_2O_7$	Tetragonal	1 1 8	45.8863 °
Ba_2SnO_4	Tetragonal	2 0 2	45.9919 °

3.2 Absorption coefficient of $BaSnO_3$ thin film

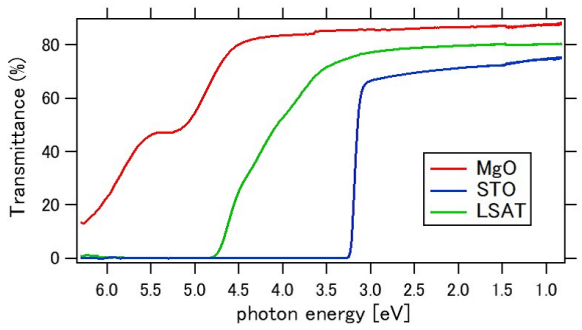

Figure 3.4: Optical transmittance spectra of double-side polished MgO, LSAT, and $SrTiO_3$ substrates.

The calculation and experimental results of optical absorption properties of $BaSnO_3$ thin film is discussed in this Section. Fig. 3.4 shows the transmittance spectra of double-side polished MgO, LSAT, and $SrTiO_3$ substrates. The MgO substrate has the largest optical band gap among these substrate materials. MgO is thus a suitable material for optical absorption measurement of $BaSnO_3$ films.

$BaSnO_3$ films were grown on double-side-polished MgO substrates. The thickness measured by XRF was 126 nm. Fig. 3.5 shows the XRD patterns and AFM images of the $BaSnO_3$ films grown on double-side MgO substrate at 800°C and 30 mTorr for the optical measurements. Only (001) orientation peaks of $BaSnO_3$ can be observed in Fig. 3.5(a), which indicates that the film is grown epitaxially on MgO. The surface roughness is about 15 nm, which is small enough to not affect the reflectance at the film surface. Fig. 3.6(a) shows the transmittance spectra of samples measured before and after $BaSnO_3$ film deposition on MgO substrates. If the reflectance at the film surface is neglected, the transmittance and absorption coefficient spectra of the $BaSnO_3$ film can be calculated with the help of the following equation

$$T_{\text{film}} = \frac{T_{\text{sub+film}}}{T_{\text{sub}}}, \tag{3.1}$$

$$\alpha = -\frac{1}{d}\ln(T_{\text{film}}). \tag{3.2}$$

The calculation results are shown in Figs. 3.6(b,c). The oscillation of the transmittance spectrum of the $BaSnO_3$ film (Fig. 3.6(b)) below 4 eV is caused by the film thickness interference fringes of the film. The film thickness can be estimated from this oscillation period using the following equations

$$2n_1 d = m\lambda_1, \tag{3.3}$$

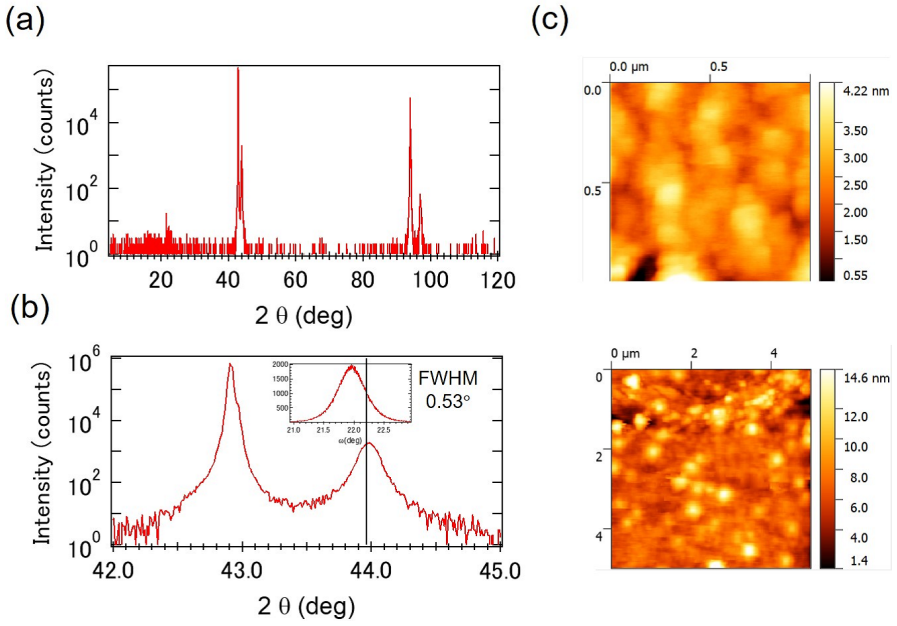

Figure 3.5: XRD patterns and AFM images of $BaSnO_3$ films grown on double-side polished MgO: (a) wide scan (b) narrow scan of (002) peaks, and (c) AFM images.

$$2n_2d = (m + \frac{1}{2})\lambda_2, \tag{3.4}$$

where n_1 and n_2 are the refraction indices for λ_1 and λ_2, d is the film thickness, m is an integer, and λ_1 and λ_2 are the wavelengths at which the transmittance reaches a local minimum and maximum, respectively. When λ_1 = 865 nm (1.43 eV) and λ_2 = 445 nm (2.79 eV), n_1 = 1.9, and n_2 = 2, [12], the calculated film thickness d is 128 nm. This calculated result is in good agreement with the thickness measured by XRF. The absorption coefficient value of $BaSnO_3$ is in reasonable agreement with the result of spectroscopic ellipsometry reported by Chambers et al., in which a $BaSnO_3$ film was grown on a $SrTiO_3$ substrate by MBE [12]. The indirect and direct band gaps of $BaSnO_3$ were determined by constructing Tauc plots [44] as shown in Figs. 3.6(d,e). The fitting gave the indirect band gap and direct band gap of 2.94 eV and 3.48 eV, respectively. This indirect band gap value is in good agreement with the band gap reported Chambers [12] and by Kim [10] for $BaSnO_3$ single crystal specimens. The direct band gap is in good agreement with the bandgap value reported by Liu [11] for a $BaSnO_3$ film grown on a MgO substrate by PLD. However agreement is not as good with the reports of 3.1 eV by Kim [10] and 3.57 eV by Chambers [12]. This disagreement with the results reported by Kim [10] probably comes from the broader spectral range of my absorption data, which allows me to identify a linear region inaccessible for Kim et al. [10].

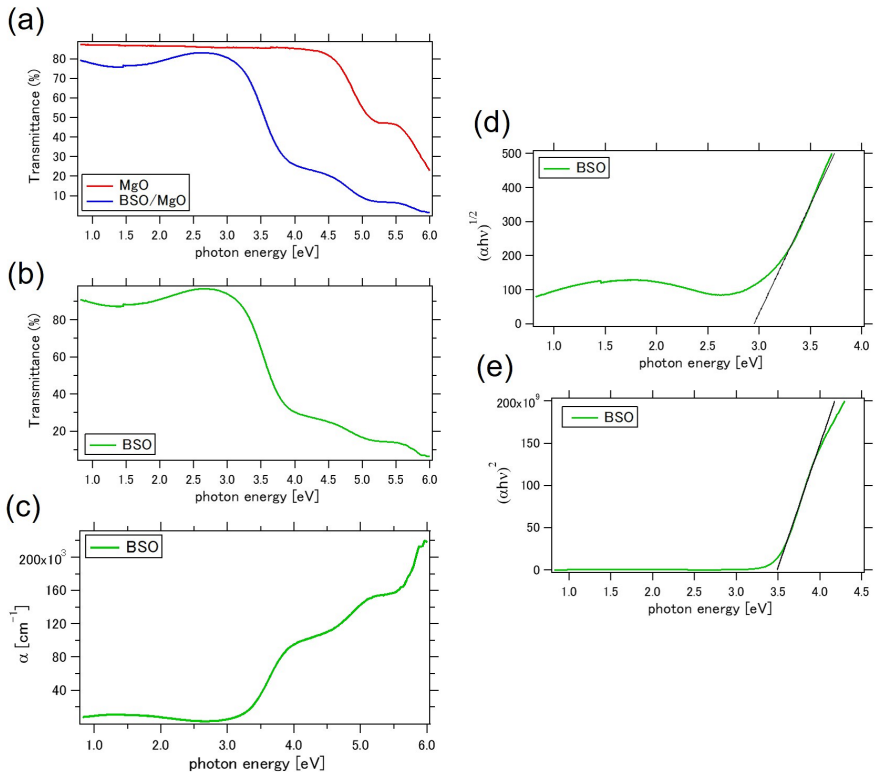

Figure 3.6: Optical properties of $BaSnO_3$: (a) transmittance spectra of MgO and $BaSnO_3$/MgO, (b) transmittance spectrum of the $BaSnO_3$ film, (c) absorption coefficient spectrum of the $BaSnO_3$ film, (d) plot of the indirect band gap, and (e) plot for the direct band gap.

From these experiments and calculations, the reasonable optical properties of $BaSnO_3$ were obtained. The obtained absorption coefficient spectrum was used for TOF measurement and photoelectrochemical measurement.

3.3 Time-of-flight measurement for $BaSnO_3$ thin films

3.3.1 Time-of-flight measurement setup

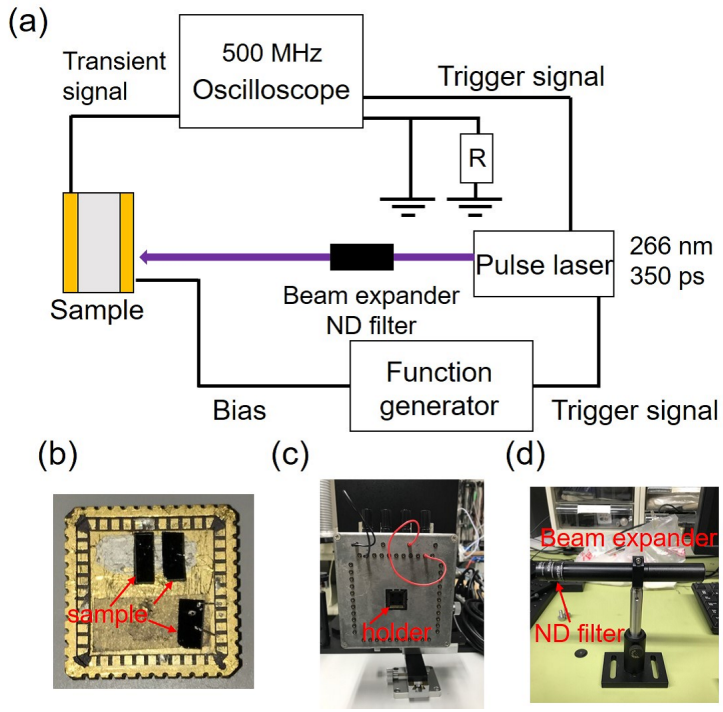

Figure 3.7: (a) Schematic illustration of the TOF carrier mobility measurement system. (b) Picture of typical samples mounted on a ceramic package. (c) Picture of a XYZ sample stage used for laser positioning. (d) Picture of the beam expander and ND filters.

In this section, a self-made time-of-flight (TOF) measurement setup is introduced. Fig. 3.7(a) shows a schematic illustration of the measurement system. thin film samples with patterned electrodes were mounted on 44-pin ceramic packages (PB-44713-N, Kyocera), and wires were attached from the electrode pads to the edge contacts of the ceramic package (Fig. 3.7(b)). The ceramic packages were mounted in a holder on a XYZ stage to measure the transient signal under pulsed laser light irradiation (Fig. 3.7(c)). A frequency-quadrupled Nd:YAG laser (Teemphotonics, PNU-M01210) operating at a wavelength of 266 nm was used for inducing free carriers in the samples. The photon energy of 4.7 eV is larger than the band gap of all samples used in this work. The laser produced 12 μJ pulses with a pulse length of 350 ps and a maximum repetition rate of 1 kHz. The repetition rate of the laser was controlled with a function

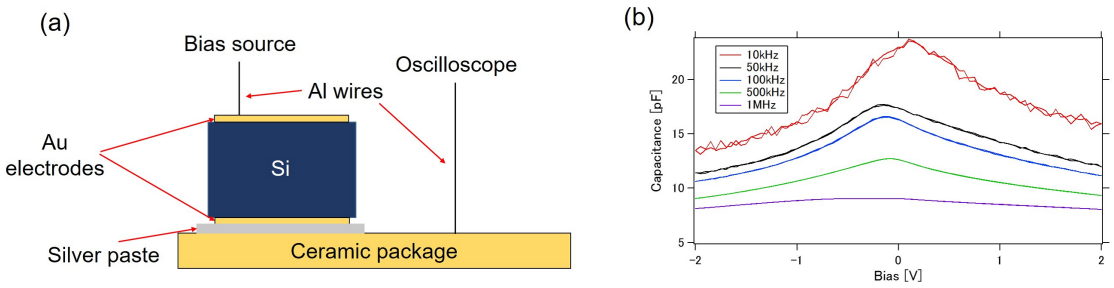

Figure 3.8: (a) Schematic illustration of the Si sample structure used in TOF test measurement. (b) Capacitance plots of the Si sample.

generator (NF, WF1944B). The spot size and the laser pulse energy were adjusted with the help of a beam expander and neutral density (ND) filters (Fig. 3.7(d)). The beam expander consists of 2 lenses, one with positive focal length of 100 mm and another one with a negative focal length of -20 mm (Galilean beam expander). Expansion of the $\sim$ 100 μm Gaussian beam width of the laser was necessary to ensure that the laser energy density incident on the sample surface remains below the damage threshold of the thin film samples. The ND filters with the optical density (OD) of 0.5, 1, 2 were used. A bias voltage was applied to top electrode of a sample with another function generator (NF, WF1944B). The voltage through the resistance placed in series with the sample was measured as a function of time with a storage oscilloscope (Tektronix, TDS3054B). The oscilloscope analog front end bandwidth is 500 MHz. Together with the 350 ps pulse length of the laser, the bandwidth of the oscilloscope sets the time resolution of the measurement.

Before drift mobility measurement of $BaSnO_3$ thin films, the drift mobility of a Si single crystal was measured as a test to validate the experimental setup. High-resistance (10 to 20 kΩcm) 500 μm thick Si single crystal wafers were bought from University Wafer, Inc. The penetration depth of the Nd:YAG laser light at 4.7 eV is about 5 nm in Si, which is much shorter than the wafer sample thickness [45]. Fig. 3.8(a) shows a schematic illustration of the sample structure for this measurement. Gold metal electrodes were deposited on both side of the Si single crystal by vacuum vapor deposition. The Si sample was attached to the bottom of a gold-plated ceramic packages with silver paste to form the bottom contact. Al wires were attached to the top electrode and the bottom of the ceramics package with an ultrasonic wedge bonder (7476D, Westbond). Fig. 3.8(b) shows capacitance measurement results of the Si sample. The capacitance of the wafer was less than 20 pF for the electrode size used in the experiment. The bias dependence is caused by the symmetric Schottky junctions forming at the top and bottom Au electrode contacts with the Si wafer.

When a 50 Ω resistance was placed in series with the sample, the *RC* time constant was ~ 1 ns, matching the time resolution of the electrical and optical parts of the measurement system. The transit time of the photocarriers can be measured by the current duration method in which the *RC* time constant must be much smaller than the transit time. Figs. 3.9(a,b,c) shows transient signals measured with an oscilloscope through a 50 Ω resistance. The top electrode bias was -1, -4, or -8 V for measuring the drift mobility of electrons towards the back electrode. The plots show that the current duration became shorter as the applied electric field increased. The transit time of the photocarriers was determined by picking the center point of the transit signal tails, which correspond to the average transit time of photocarriers. The drift mobility of electrons can be obtained from the slope of a $1/t_t$ vs V/d^2 plot:

$$\frac{1}{t_t} = \mu \frac{V}{d^2}, \tag{3.5}$$

where t_t is the transit time, V is the absolute value of the applied voltage, and d is the sample thickness. From this plot, as shown in Fig. 3.9(d), the obtained drift mobility was estimated to be 50 cm^2/sV. This value is too small for the drift mobility of a Si single crystal, indicating that this result is affected by the space charge effect as discussed later.

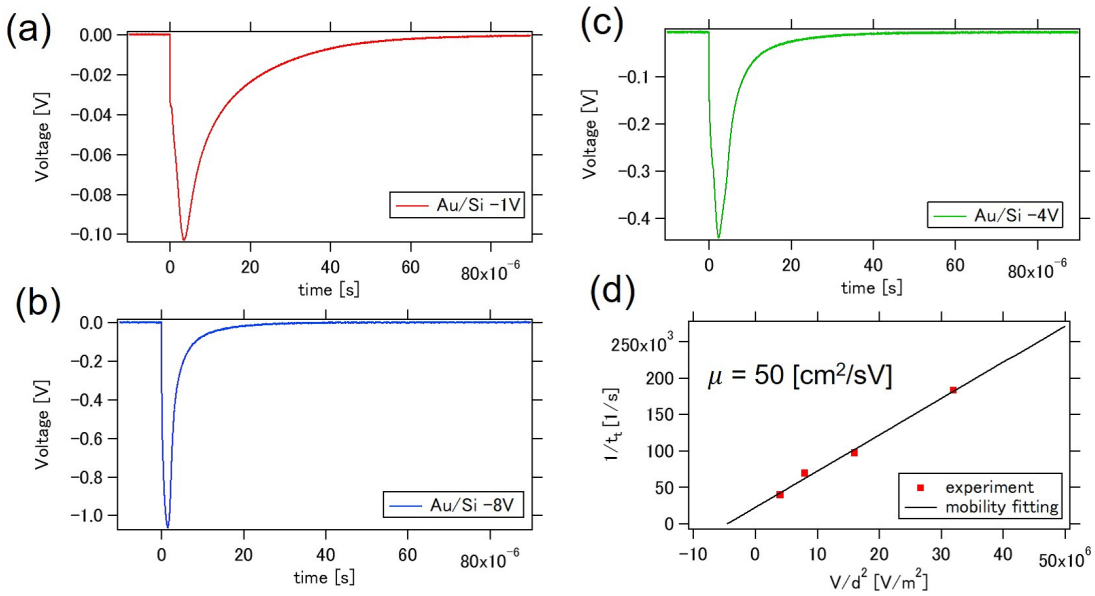

Figure 3.9: The transient signal of Si measured with an oscilloscope through a 50 Ω resistance at (a) -1V, (b) -4V, (c) -8 V bias applied to the top electrode. (d) Plot of electron drift mobility.

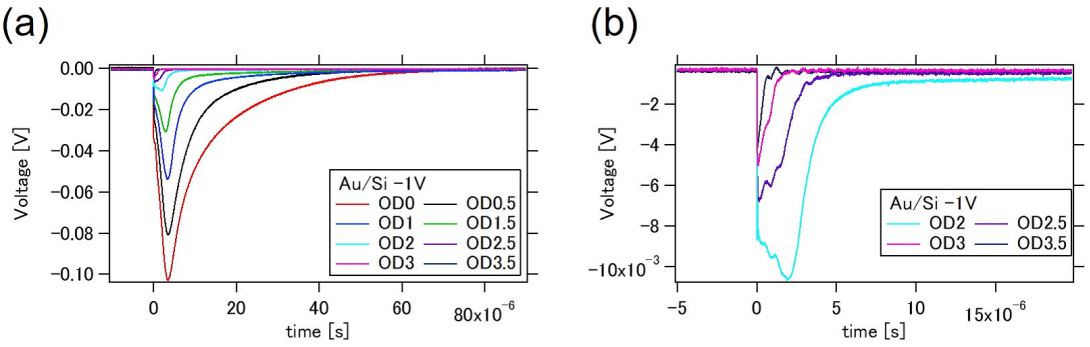

Figure 3.10: (a) Excitation laser intensity dependence of the transient signal of Si measured with a digital oscilloscope over a 50 Ω series resistance. (b) Magnified figure for the signal obtained under weak excitation.

Figs. 3.10(a,b) shows the excitation laser intensity dependence of the transient signal measured with an oscilloscope through a 50 Ω resistance. A −1 V bias was applied to the top electrode. The current pulse duration was clearly dependent on the laser intensity. The average pulse duration became shorter when the excitation laser intensity was decreased with ND filters. The signal shape also changed, becoming more rectangular when a weaker laser intensity was used as shown in Fig. 3.10(b). This kind of behavior is known as space charge limited current. [46, 47] When the photo-generated carrier charge q is much larger than the charge on the electrode of condenser Q, a large carrier reservoir is generated close to top electrode and only a small part of photo-generated carriers are injected into the bulk semiconductor at any one time. To measure the average transit time of photocarrier, all the photocarrier must be injected into the bulk at the same time. The photo-generated carrier charge q can be calculated by integration the transient current signal. The obtained value was shown in table 3.4. Obviously, q is much larger than the charge on the electrode of the condenser Q (C = 20 pF), providing a long current duration. Due to the space charge effect, a sufficiently weak excitation should be used to measure the correct drift mobility.

Table 3.4: The photo-generated carrier charge calculated by integrating the transient current signal.

ND filter	q [C]	ND filter	q [C]
OD0	2.9×10^{-8}	OD2	1.0×10^{-9}
OD0.5	1.7×10^{-8}	OD2.5	3.7×10^{-10}
OD1	8.2×10^{-9}	OD3	8.8×10^{-11}
OD1.5	3.9×10^{-9}	OD3.5	4.0×10^{-12}

Figs. 3.11(a,b) show the bias dependence of the transient signal, measured with OD2.5 and OD3 ND filters, respectively. The applied bias on the top electrode is shown in the labels of each figure. The transit time of photocarriers was determined by picking the center point of the transit signal tails, marked by black lines. The drift mobility of electrons was obtained from the slope of a $1/t_t$ vs V/d^2 plot. Figs. 3.11(c,d) show these plots for two excitation intensities. The obtained drift mobilities are 499 cm^2/sV and 1248 cm^2/sV for excitation with OD2.5 and OD3 filters, respectively. The reported electron mobility of Si at room temperature is about 1400 cm^2/sV. [48] The drift mobility obtained with the OD3 filter is in good agreement with the reported value of electron mobility in Si. From this test measurement, it was concluded that the self-made TOF measurement system works as intended.

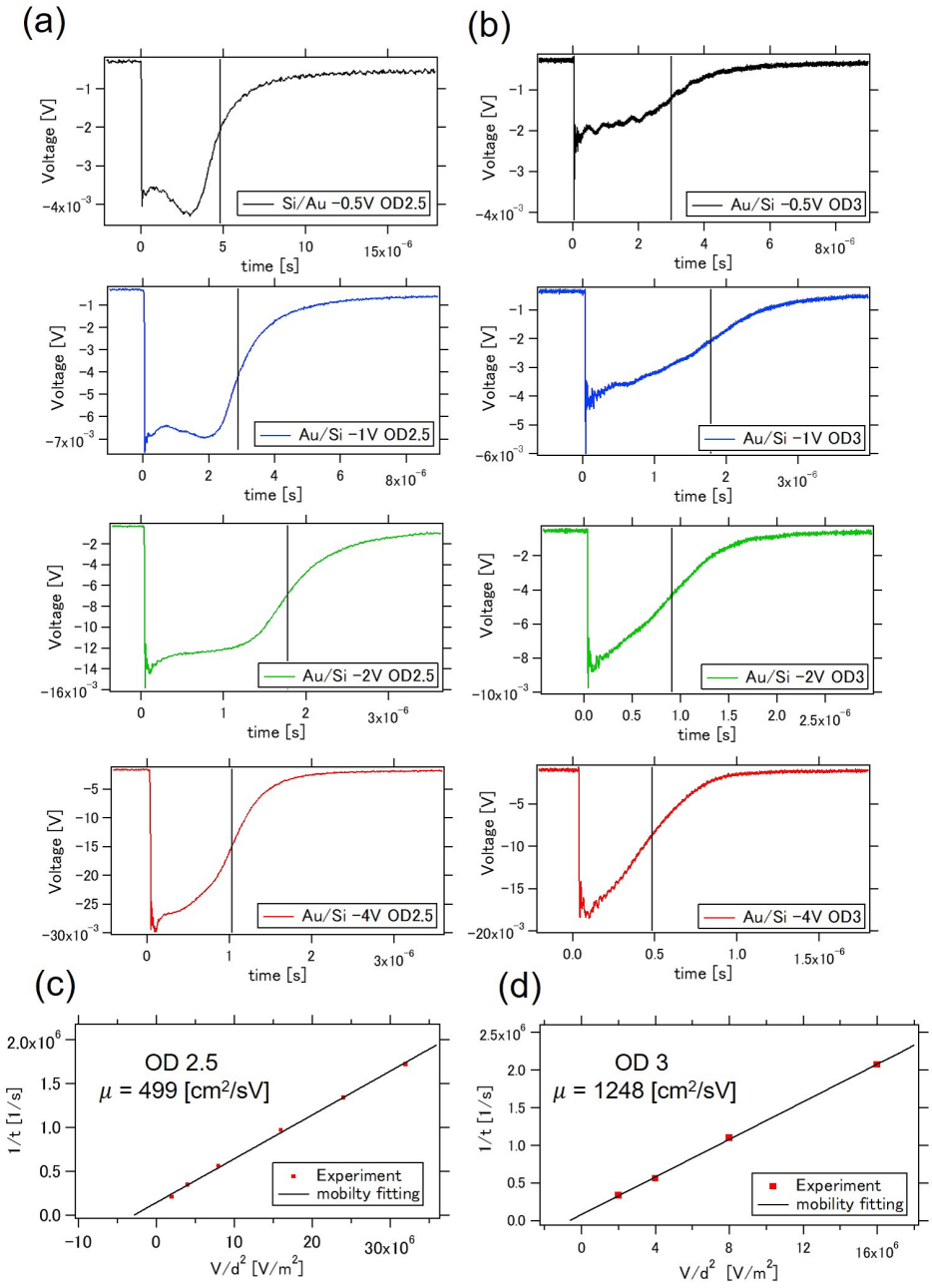

Figure 3.11: Bias dependence of transient signals measured with attenuated laser light through (a) OD2.5 and (b) OD3 filters. Plots for electron drift mobility for (c) OD2.5 and (d) OD3 laser excitation.

3.3.2 $BaSnO_3$ sample preparation

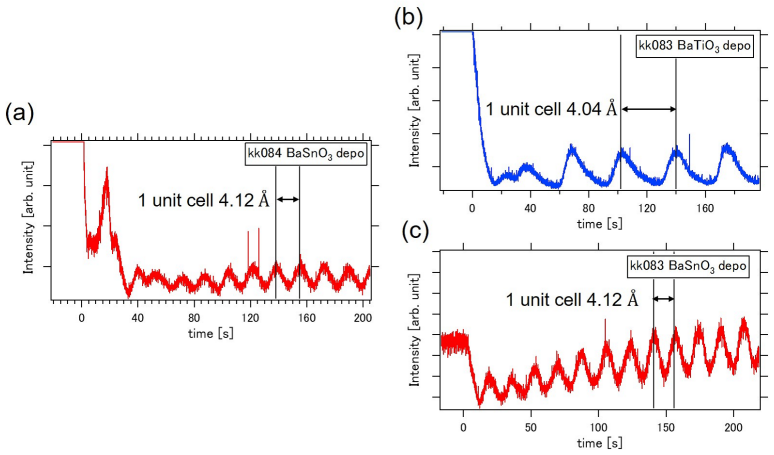

Figure 3.12: Typical RHEED oscillation behavior during (a) $BaSnO_3$ deposition on Nb-doped $SrTiO_3$, (b) $BaTiO_3$ deposition on Nb-doped $SrTiO_3$, and (c) $BaSnO_3$ deposition on $BaTiO_3$.

$BaSnO_3$ thin films were grown on 0.5wt% Nb-doped $SrTiO_3$ substrates at 750°C and an oxygen pressure of 30 mTorr. The film thickness of $BaSnO_3$ was estimated by measuring the RHEED specular intensity oscillation period length. Fig. 3.12(a) shows typical RHEED oscillations during $BaSnO_3$ deposition. Periodic intensity oscillations can be observed after an initial growth of a few unit cells. The non-periodic behavior during initial growth is probably related to the large lattice mismatch between the film and the substrate. The oscillation period corresponds to the growth of one $BaSnO_3$ (4.12 Å) unit cell layer. The 0.5wt% Nb-doped $SrTiO_3$ substrates have sufficiently low resistivity to be used as metallic bottom electrodes in TOF experiments.

$BaSnO_3$ thin films were also grown on $BaTiO_3$ buffer layers to decrease the lattice mismatch and possibly improve the film crystallinity and grain structure. $BaTiO_3$ has tetragonal perovskite structure with the lattice parameters of $a = b = 3.994$ Å and $c = 4.038$ Å. [49] The in-plane lattice mismatch between $BaTiO_3$ and $BaSnO_3$ is 3.0%. In-plane lattice constant tuning using $BaTiO_3$ buffer layers has been reported by Terai, et al. [50]. In this paper, a strained 30 nm $BaTiO_3$ film was grown on a $SrTiO_3$ substrate at 650°C. After deposition, an atomically smooth surface and a fully relaxed $BaTiO_3$ film were regained by vacuum annealing at 1100°C in 10^{-6} Torr of oxygen.

The same method was used in this work to decrease the lattice mismatch between the $BaSnO_3$ film and a Nb-doped $SrTiO_3$ substrate. $BaTiO_3$ films were grown on Nb-doped $SrTiO_3$ substrates at 650°C at several oxygen pressures. The thickness of the $BaTiO_3$ films was adjusted to 20 nm by counting RHEED oscillations as shown in

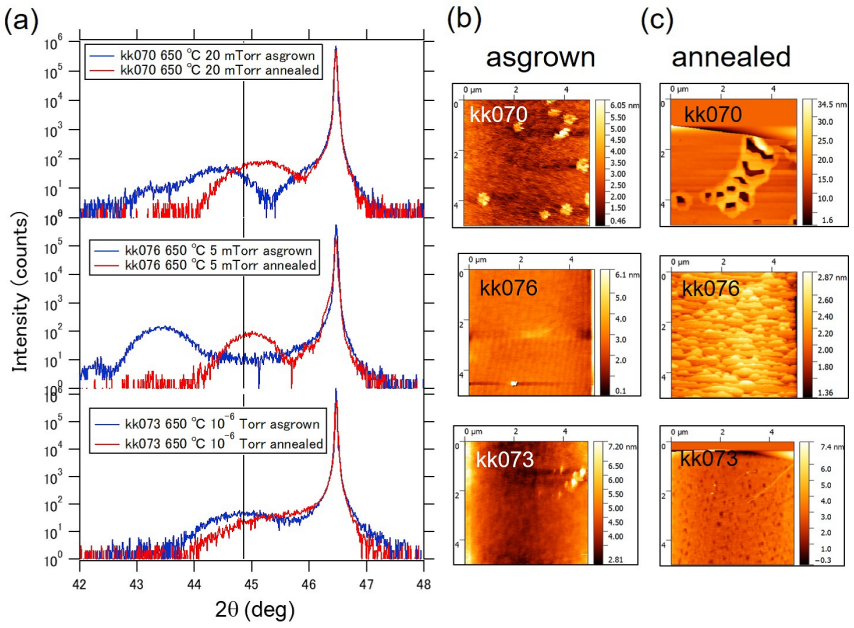

Figure 3.13: (a) The narrow XRD scans around the (002) peak of the as-grown $BaTiO_3$ films while the blue lines show the XRD patterns of the $BaTiO_3$ films taken after anneal the samples for 1 hour at 1100°C in 10^{-6} Torr of oxygen. (b,c) the AFM images of $BaTiO_3$ films before and after high-temperature annealing..

Fig.3.12(b). The red plots in Fig. 3.13(a) show a narrow XRD scans around the (002) peak of the as-grown $BaTiO_3$ films while the blue lines show the XRD patterns of the $BaTiO_3$ films taken after anneal the samples for 1 hour at 1100°C in 10^{-6} Torr of oxygen. The films grown in 5 mTorr and 20 mTorr were originally strained after growth and relaxed after vacuum annealing, similar to the report by Terai et al. [50]. Figs. 3.13(b,c) show the AFM images of these films before and after high-temperature annealing. A step and terrace surface can be seen in the surface image of film grown at 5 mTorr. This surface is smooth enough for use as a buffer layer.

A 750 nm thick $BaSnO_3$ film was grown at 750°C at an oxygen pressure of 30 mTorr on a $BaTiO_3$ buffer layer grown at 5 mTorr. The RHEED oscillations during the $BaSnO_3$ deposition on the $BaTiO_3$ buffer layer is shown in Fig.3.12(c). A clear intensity oscillation was obtained when $BaSnO_3$ was grown on a $BaTiO_3$ buffer layer because of a better lattice match than with the Nb-doped $SrTiO_3$ substrate. However, the crystallinity of the $BaSnO_3$ film on a $BaTiO_3$ buffer layer was worse than without a buffer. Figs. 3.14(a,b) show the narrow scan XRD patterns around the (002) peaks and the rocking curves of the (002) peaks of the $BaSnO_3$ films grown directly on a Nb-doped $SrTiO_3$ substrate and on a $BaTiO_3$ buffer layer. Even though $BaTiO_3$ has a better lattice

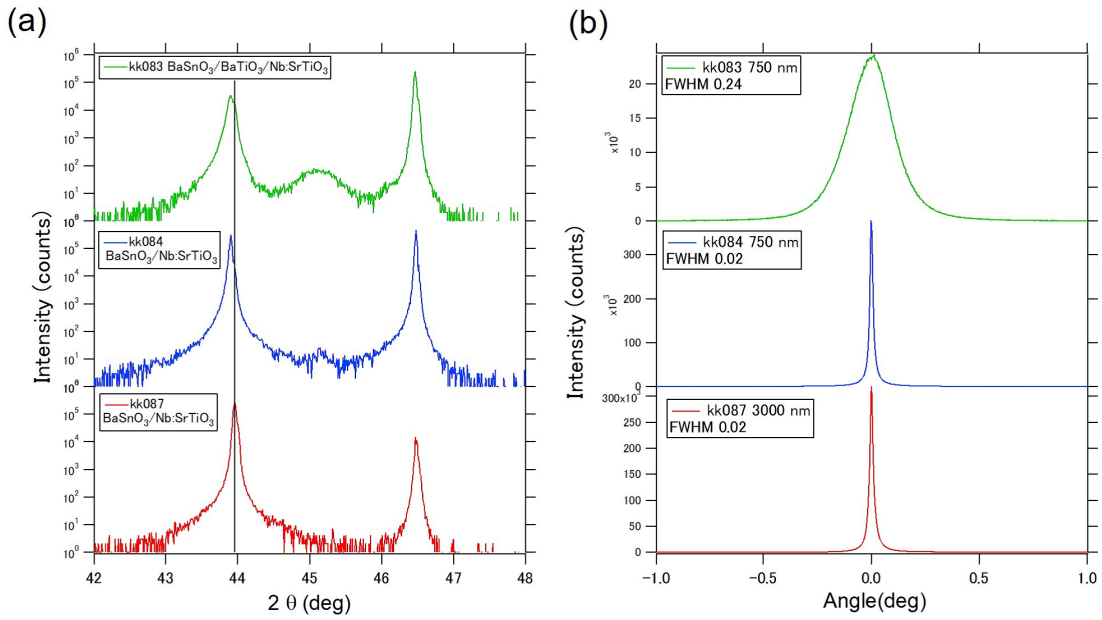

Figure 3.14: Narrow scan XRD patterns around the (002) peaks and rocking curves of the (002) peaks of $BaSnO_3$ films grown on Nb-doped $SrTiO_3$ and on a $BaTiO_3$ buffer layer.

match with $BaSnO_3$, the FWHM of the rocking curve of the film grown on the $BaTiO_3$ buffer (shown in green) was an order of magnitude broader than the rocking curve of a film grown directly on the $SrTiO_3$ substrate (blue plot). The reason for this result is not clear.

In conclusion, thick $BaSnO_3$ films grown directly on Nb-doped $SrTiO_3$ substrates were used for time-of-flight measurements. Semitransparent Au top electrodes were deposited on the film surface by vacuum evaporation. The samples were attached to ceramic packages and metal wires were attached to the top electrodes with silver paste and to the substrates with an ultrasonic wedge bonder (7476D, Westbond) as shown in Fig. 3.15(a). In total, 6 $BaSnO_3$ films were prepared on Nb-doped $SrTiO_3$. The best results were obtained from sample kk084 for which the XRD data is shown in blue in Fig. 3.14. The measurement details for this sample and for the thickest sample, kk087 (shown in red in Fig. 3.14), are discussed in Chapter 3.3.3. The crystallinity of these films was very good as seen from the rocking curves in Fig. 3.14.

.

3.3.3 Drift mobility of $BaSnO_3$ thin films

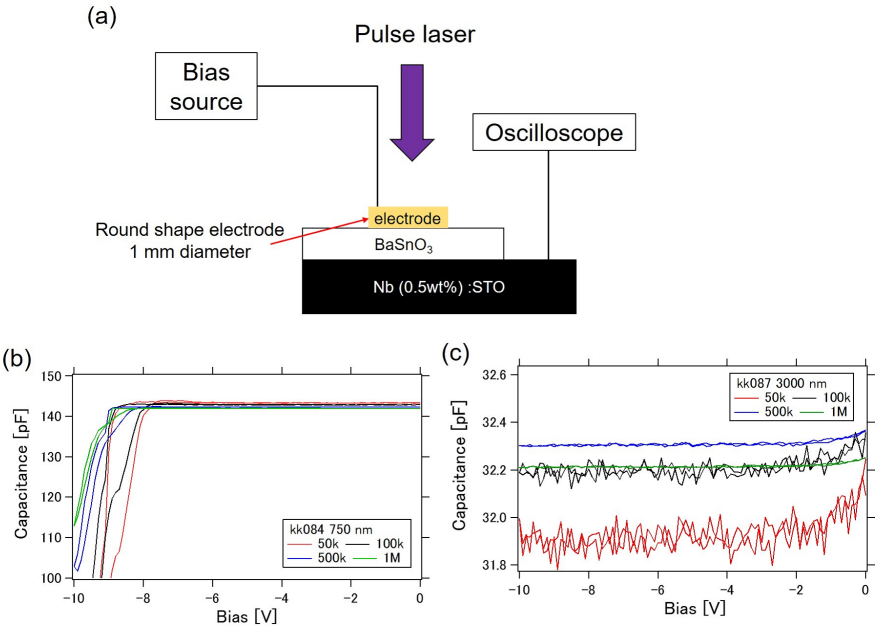

Figure 3.15: (a) $BaSnO_3$ sample structure for time-of-flight measurement, (b,c) Capacitance vs bias measurements of two $BaSnO_3$ samples.

A 500 MHz oscilloscope was used in my measurement setup to measure the transient current signals. The oscilloscope analog bandwidth thus sets the time resolution of this measurement setup to the order of 10^{-9} s. If the lifetime of photocarriers is less than 1 ns, it is impossible to measure the drift mobility of photocarriers by the TOF method. Figs.3.15(b,c) show the capacitance measurement results for two $BaSnO_3$ films. The capacitance of the 750 nm thick sample (kk084) and 3000 nm thick sample (kk087) are about 140 pF and 30 pF, respectively. The capacitance of the 750 nm film rapidly decreases at high bias of over -8 V due to breakdown. When a 50 Ω resistance was placed in series with the sample, the *RC* time constants are about 7 ns and 1.5 ns. Therefore taking the *RC* time constants into consideration, for accurate measurement, it is desirable for the transient time of photocarriers to be much longer, on the order of 10 ns.

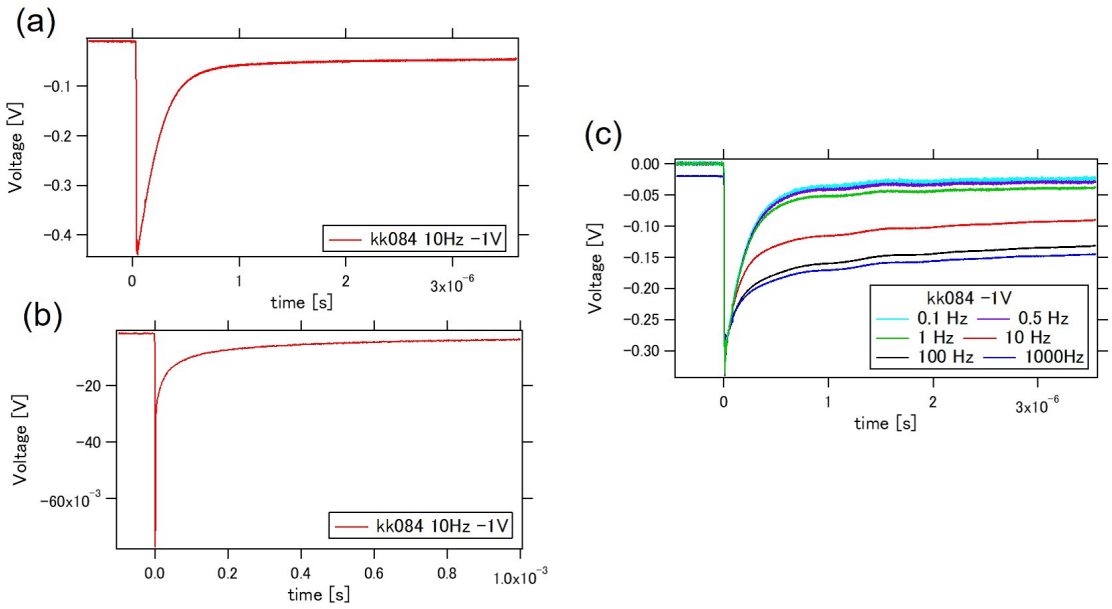

Figure 3.16: Transient signal shapes of $BaSnO_3$ films in the (a) microsecond and (b) millisecond time scales. (c) The excitation frequency dependence of the transient signal shapes.

Figs. 3.16(a,b) shows the transit signal of the 750 nm $BaSnO_3$ samples (kk084) measured with a 50 Ω series resistance and a -1 V bias applied to the top electrode. The signal shape is different from the silicon test sample case and the measured current shows a very long, millisecond scale decay tail. This time response is too long for this signal to represent carrier diffusion. Instead, this time constant reflects the trapped carrier lifetime in $BaSnO_3$, possibly affected by carrier hopping under the applied bias. Fig. 3.16(c) shows the excitation laser repetition rate dependence of the transit signal for the same sample. The signal decay time is clearly repetition rate dependent, with longer decay times being observed for higher laser repetition rates. This behavior is consistent with photocarrier trapping. The growing relaxation tail represents carriers accumulated in trap states when trap states do not fully relax by recombination before the next excitation pulse. To exclude the trapped carriers effect on the transit signal, the excitation laser frequency was set to 0.1 Hz in the following experiment.

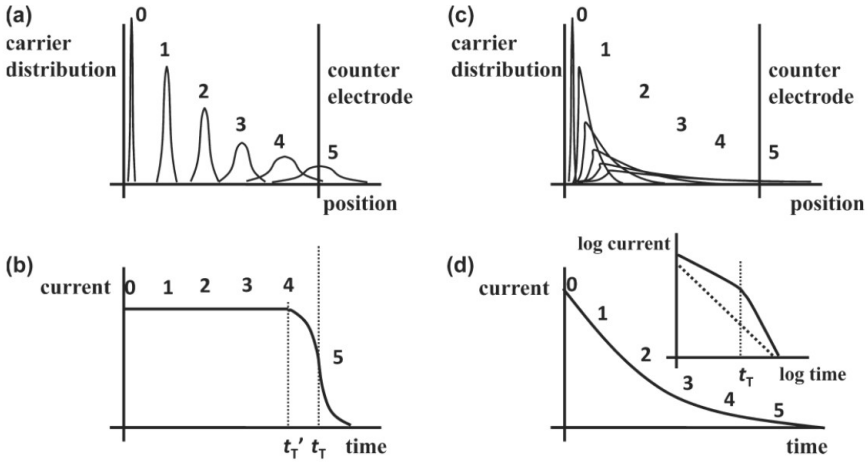

Figure 3.17: (a) Distribution of photocarriers in a sample with non-dispersive transport, (b) current signal for non-dispersive transport, (c) distribution of photocarriers in sample with dispersive transport and (d) current signal for dispersive transport. [47]

This kind of signal shape is known as a dispersive current signal. Fig. 3.17 shows the schematics of distribution of photocarriers and current signals for non-dispersive transport (a,b) and dispersive transport (c,d) obtained by TOF measurement. [47] In the case of Si, the photocarriers can drift to the bottom electrode without trapping because of high-crystallinity and long carrier lifetime, leading to a Gaussian packet of photocarriers as shown in Fig. 3.17(a) and a rectangle current shape as shown in Fig. 3.17(b). On the other hand, the current shapes shown in Fig. 3.17(d) are obtained in many semiconductor materials. [25, 26, 51] This kind of current shape reflects the presence of various trap states with different trap depths in the sample material. Some of the photocarriers drift without trapping or detrapping while most of the photocarriers are trapped as shown in Fig. 3.17(c). The transit time of photocarriers cannot therefore be clearly observed. In this case, a kink may appear in a $\log(t) - \log(V)$ plot as shown in the inset of Fig. 3.17(d). When the position of the kink is dependent on the magnitude of the bias, the position of the kink can be considered as the transit time of photocarriers. [47, 52]

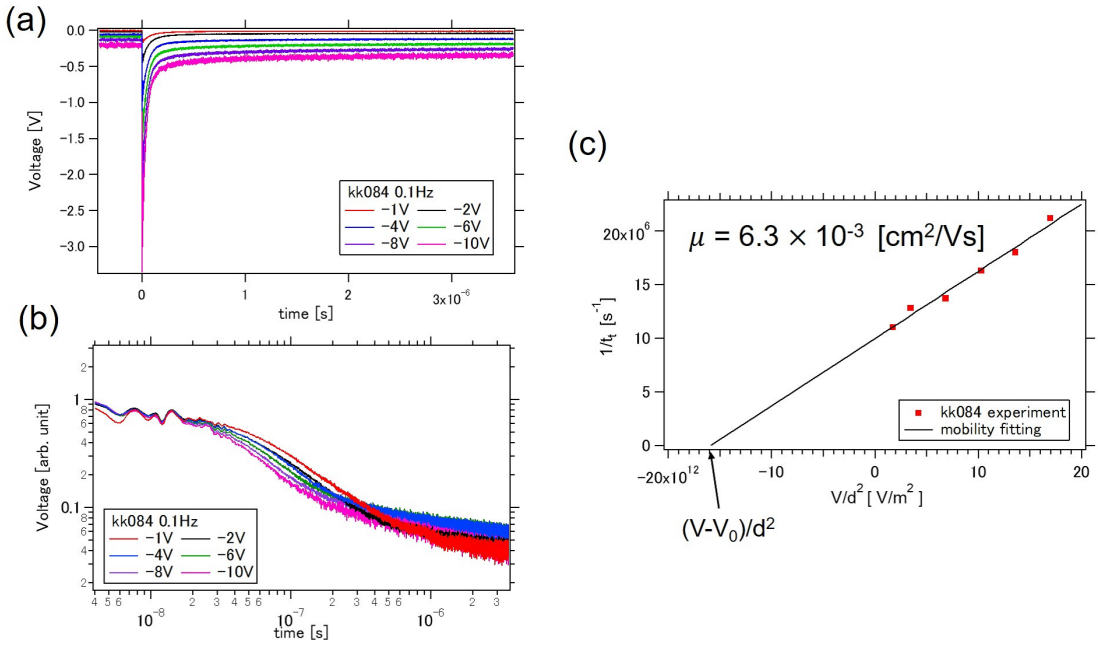

Figure 3.18: The applied bias dependence of transient signals of the 750 nm $BaSnO_3$ sample on (a) a linear scale and (b) normalized transient signals in a $\log(t) - \log(V)$ plot. (c) Plot of electron drift mobility.

Figs. 3.18 (a,b) show the applied bias dependence of transit signals of the same sample on a linear scale and the normalized transient signals in a $\log(t) - \log(V)$ plot. The bias-dependent kinks can be observed in Fig. 3.18(b). From the slope of a $1/t_t$ vs V/d^2 plot using these kink positions, the drift mobility of electron can be calculated as 6.3×10^{-3} cm^2/sV as shown in Fig. 3.18(c). This mobility is much smaller than the reported Hall mobility (70 cm^2/sV) of La-doped $BaSnO_3$ films grown on $SrTiO_3$. [14] There are two reasons that may cause this difference. The dominant reason is probably space charge effect. Strong excitation may cause the space charge limited current like in the case of Si as shown in Chapter 3.3.1. The photogenerated carrier charge should be on the order of 10^{-8} C. This is much bigger than the charge on the electrode of the condenser (140 pF). And the fitting line in Fig. 3.18 (c) doesn't pass through origin. The applied bias appears to be increased by the constant amount of V_0 = 9 V. This increased bias can be seen in the case of Si and the amount of the bias become small as the laser intensity decrease as shown Figs 3.9 (d) and 3.11 (c,d). It means this is caused by space charge effect: when a large carrier reservoir is generated close to top electrode, the holes are rapidly drawn out to top electrode applied negative bias and the electrons remain. Only a small part of this electrons are injected into the bulk semiconductor at any one time because q is much bigger than Q. This electron reservoir may cause

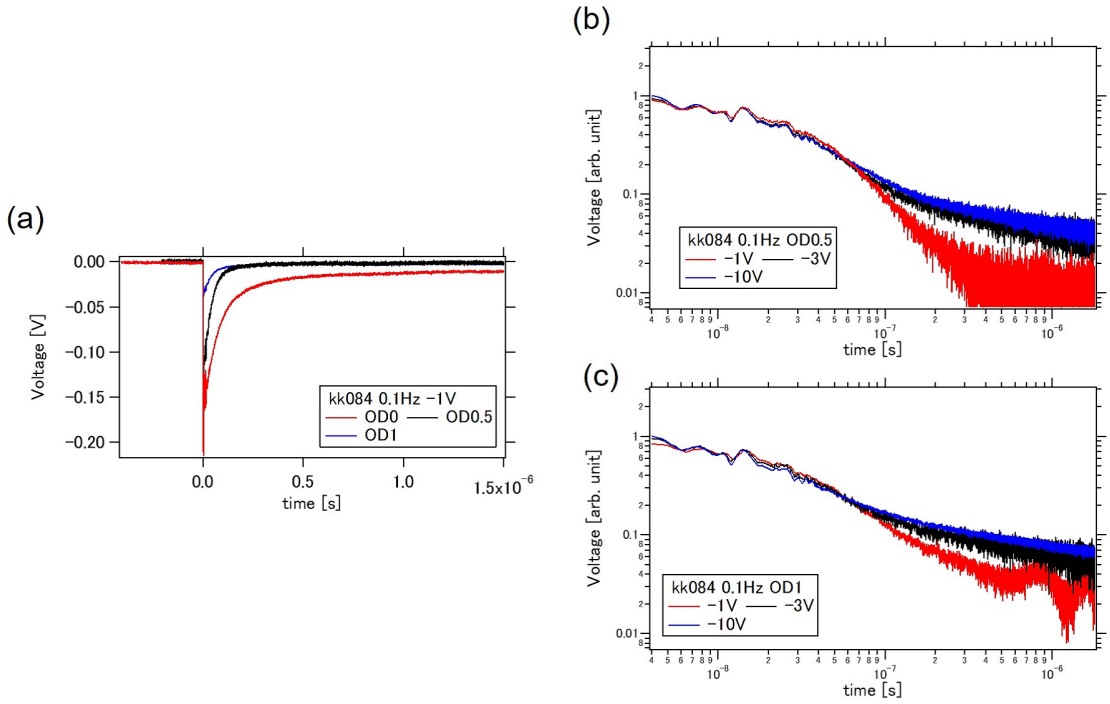

Figure 3.19: (a) Transient signals of the 750 nm $BaSnO_3$ sample with an ND filter on a linear scale. (b,c) Normalized transient signals of the $BaSnO_3$ sample with ND 0.5 and 1 filters on a double logarithmic scale.

increased applied bias. Although the situation is different from this measurement, the applied bias reduction due to space charge effects was reported by W. E. Spear for Se in hole mobility measurement by TOF [53]. Accordingly, A weak intensity of excitation laser should be used. Fig. 3.19(a) shows the transient signals of the same sample with an ND filter in a linear plot. The duration of transient signals become shorter as the laser intensity become weaker. However the bias dependent kinks cannot be observed in $\log(t) - \log(V)$ plots as shown Figs. 3.19(b,c), indicating that photocarriers cannot reach the bottom electrode due to heavy trapping and short carrier lifetime.

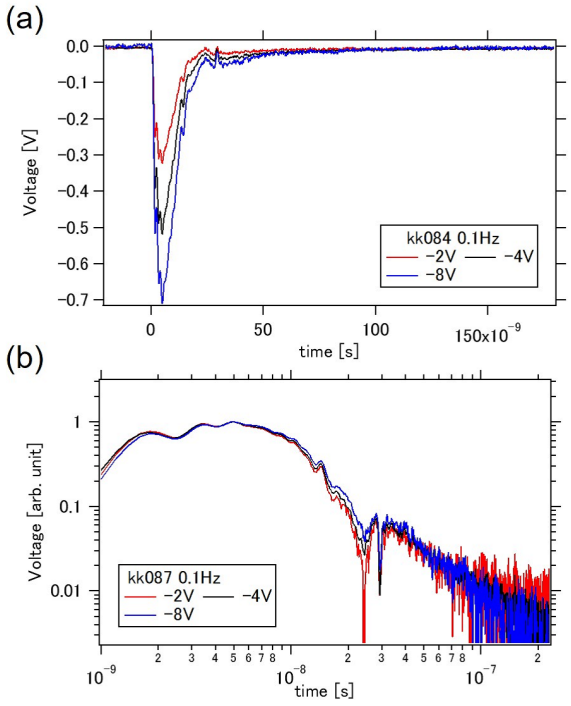

Figure 3.20: (a) The applied bias dependence of the transient signals of the 3 μm $BaSnO_3$ sample on a linear scale. (b) Normalized transient signals in a double logarithmic plot.

Another reason is the insufficient film thickness of $BaSnO_3$. As mentioned in Chapter 2.6, the penetration depth of the excitation laser must be much smaller than the sample thickness. However, the film thickness and penetration depth of the laser are 750 nm and about 80 nm, respectively. A suitable sample thickness for time-of-flight measurement is usually more than 10 times larger than the penetration depth. [26, 54]. The film thickness of $BaSnO_3$ may not be sufficient compared to the penetration depth. To test this assumption, the transient signals of a 3 μm $BaSnO_3$ film (kk087) were measured. Fig. 3.20(a) shows the transient signals of the 3 μm $BaSnO_3$ film in a linear plot. A very short current durations of less than 100 ns were observed, even though strong excitation was used. The corresponding $\log(t) - \log(V)$ plot is shown in Fig. 3.20(b). The bias dependent kinks cannot be observed. These results indicate the none of the photocarriers reach the bottom electrode due to a short lifetime.

From these results, I conclude that it is impossible to measure the correct drift mobility of photocarriers in $BaSnO_3$ thin film with this TOF setup due to heavy trapping and short trapping lifetime. The transient signals recorded by the oscilloscope are limited by the short lifetime of carriers and hence no long-range charge migration takes place before the loss of the photoexcited carriers. In other words, the diffusion length

of photocarriers in the $BaSnO_3$ thin film is much smaller than the film thickness. The obtained electron drift mobility was 6.3×10^{-3} cm^2/sV. This value is thus not indicative of the true carrier mobility due to space charge effects and rapid recombination. To evaluate the correct drift mobility, other methods such as picosecond optical time-of-flight [55] or photoelectrochemical performance analysis [56] may be useful, since carrier diffusion over nanometer distances can be determined

3.4 Photoelectrochemical analysis of $BaSnO_3$ thin films

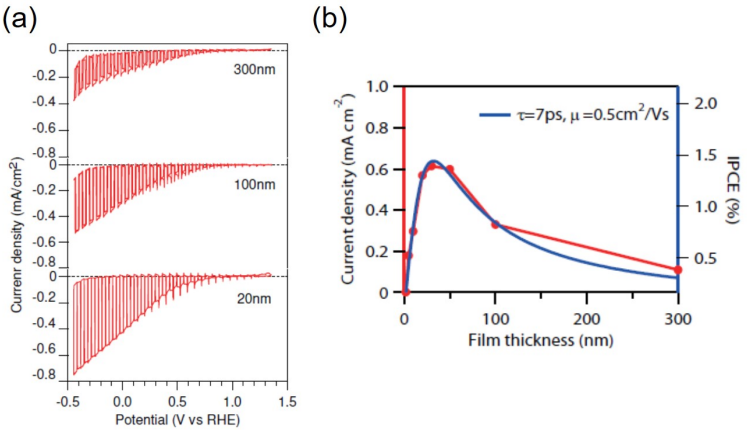

Figure 3.21: (a) Cyclic voltammetry curves of Rh-doped $SrTiO_3$ films with different thicknesses. (b) Film thickness dependence of photocurrent density at −0.25 V in cyclic voltammetry measurement (red) and a simulation result (blue). [56]

In a previous study by Kawasaki [56], it was found that the semiconductor film thickness affects the photocurrent density in cyclic voltammetry measurements. Fig. 3.21(a) shows reference data for cyclic voltammetry measurements of a Rh-doped $SrTiO_3$ film. [56] The Rh-doped $SrTiO_3$ film thicknesses were 300 nm, 100 nm, and 20 nm. This thickness dependence can be understood in terms of light absorption and charge transport efficiency. The red line in Fig. 3.21(b) shows the film thickness dependence of photocurrent density at −0.25 V vs a reversible hydrogen electrode (RHE) in cyclic voltammetry measurement and the blue line shows a simulation result of the incident photon to current efficiency (IPCE) using an analogous model used for analyzing solar cell performance [57], in which the electric field in the film was assumed to be linear [56]. From this simulation, the photocarrier lifetime and drift mobility of Rh-doped $SrTiO_3$ film were estimated. The estimated photocarrier lifetime value of 7 ps is in good agreement with the lifetime measurement result 10 ps that was obtained by measuring transient THz absorption in a pump-probe experiment [56]. In this section, the same analysis method was used to estimate the lifetime and mobility of photoexcited carriers in $BaSnO_3$.

3.4.1 Sample preparation for photoelectrochemical measurement

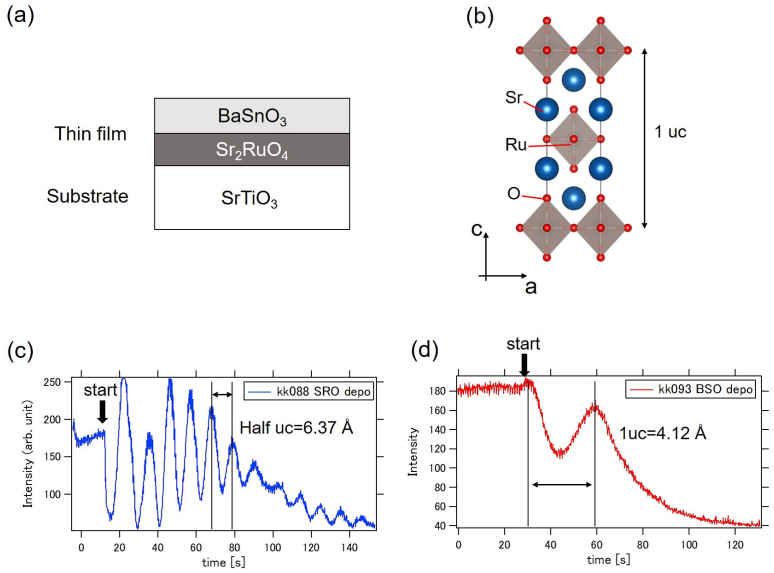

Figure 3.22: (a) Sample structure for photoelectrochemical measurement. (b) Crystal structure of Sr_2RuO_4. (c) Typical RHEED oscillation during Sr_2RuO_4 deposition and (d) during $BaSnO_3$ deposition.

In total, 7 $BaSnO_3$/Sr_2RuO_4(SRO)/$SrTiO_3$ heterostructure samples were prepared. The sample structure is shown in Fig. 3.22(a)). The only difference between samples was the $BaSnO_3$ film thickness. Sr_2RuO_4 is a metallic oxide material which has the Ruddlesden-Popper ($n = 1$) structure with lattice parameters $a, b = 3.873$ Å and $c = 12.754$ Å as shown in Fig. 3.22(b) [58]. Sr_2RuO_4 is a metallic oxide that can be used as a bottom electrode and doesn't affect the photoelectrochemical performance.

Firstly, Sr_2RuO_4 films were grown on $SrTiO_3$ substrates at 700°C at 1 mTorr. The lattice mismatch between Sr_2RuO_4 and $SrTiO_3$ is 0.82%. Fig. 3.22(c) shows the typical RHEED specular intensity oscillation behavior during the deposition of the Sr_2RuO_4 layer. The RHEED intensity oscillations correspond to the growth of half a unit cell of Sr_2RuO_4 (6.37 Å). The thickness of the Sr_2RuO_4 films were set at 20 nm by monitoring the RHEED oscillation period. After the deposition of the Sr_2RuO_4 electrode layer, $BaSnO_3$ films were grown on Sr_2RuO_4/$SrTiO_3$ at 750°C and 30 mTorr oxygen pressure. The lattice mismatch between Sr_2RuO_4 and $BaSnO_3$ is 6.3%. Fig. 3.22(b) shows typical RHEED oscillations during the initial layer deposition of a $BaSnO_3$ film on the Sr_2RuO_4 surface. The RHEED oscillation during $BaSnO_3$ deposition rapidly disappear in a few periods, indicating that the $BaSnO_3$ films were grown on Sr_2RuO_4 in a wetting layer and island growth mode due to large lattice mismatch.

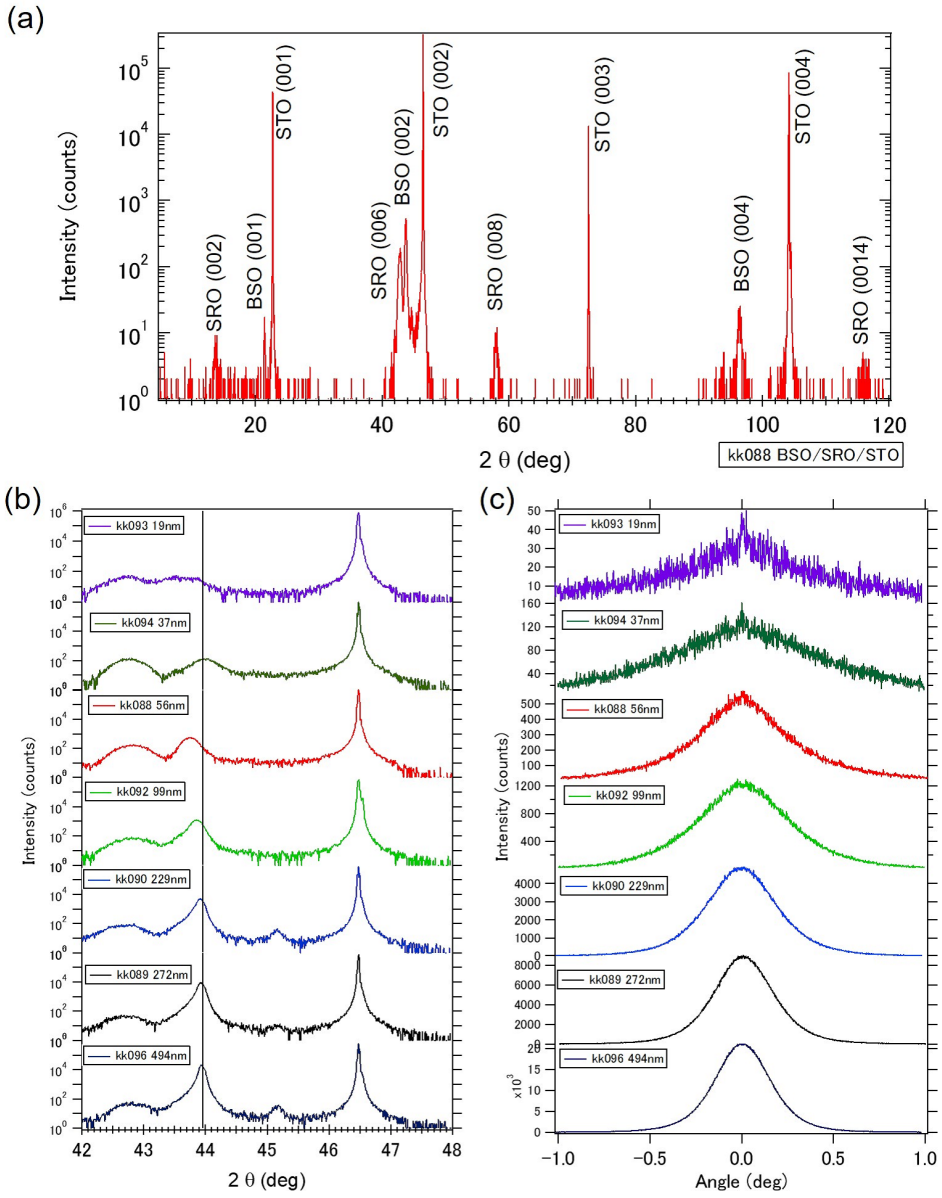

Figure 3.23: (a) A wide XRD scan of a $BaSnO_3/Sr_2RuO_4/SrTiO_3$ structure. (b) Narrow scans around the $BaSnO_3$ (002) peaks and (c) the rocking curves of the $BaSnO_3$ (002) peaks.

Fig. 3.23(a) shows a wide scan XRD pattern of the $BaSnO_3/Sr_2RuO_4/SrTiO_3$ structure. Only (00*l*) orientation peaks of $BaSnO_3$, Sr_2RuO_4 and $SrTiO_3$ were observed, which means that the $BaSnO_3$ and Sr_2RuO_4 films were grown epitaxially. Figs. 3.23(b,c) show XRD narrow scans close to the (002) peaks of $BaSnO_3$, and the rocking curves of the $BaSnO_3$ (002) peaks, respectively. The labels show the sample identification and the film thickness of each sample. The thickness and the ratio of BaO/SnO_2 was measured by XRF as shown in Table 3.5. All samples were found to be slightly Sn-rich. As shown Fig. 3.23(b), the peak position of the thinner films, except for kk094, are slightly shifted due to epitaxial strain from the expected bulk peak position, which is marked with a black line. The peak positions of thicker films are almost the same as the bulk peak position, which means that the top part of thicker films is fully relaxed. The crystallinity of thicker films is also obviously better than the thinner films as can be seen by the narrowing of the rocking curve widths as the film thickness increases. This crystallinity difference may also affect the photoelectrochemical performance.

Table 3.5: XRF measurement results of $BaSnO_3/Sr_2RuO_4$(SRO)/$SrTiO_3$ samples.

Sample	Film thickness	BaO (mol%)	SnO2 (mol%)
kk093	19 nm	48.86	51.14
kk094	37 nm	48.76	51.24
kk088	56 nm	48.83	51.17
kk092	99 nm	48.32	51.68
kk090	229 nm	48.52	51.48
kk089	272 nm	47.88	52.12
kk096	494 nm	47.65	52.35

3.4.2 Cyclic voltammetry and carrier mobility simulation

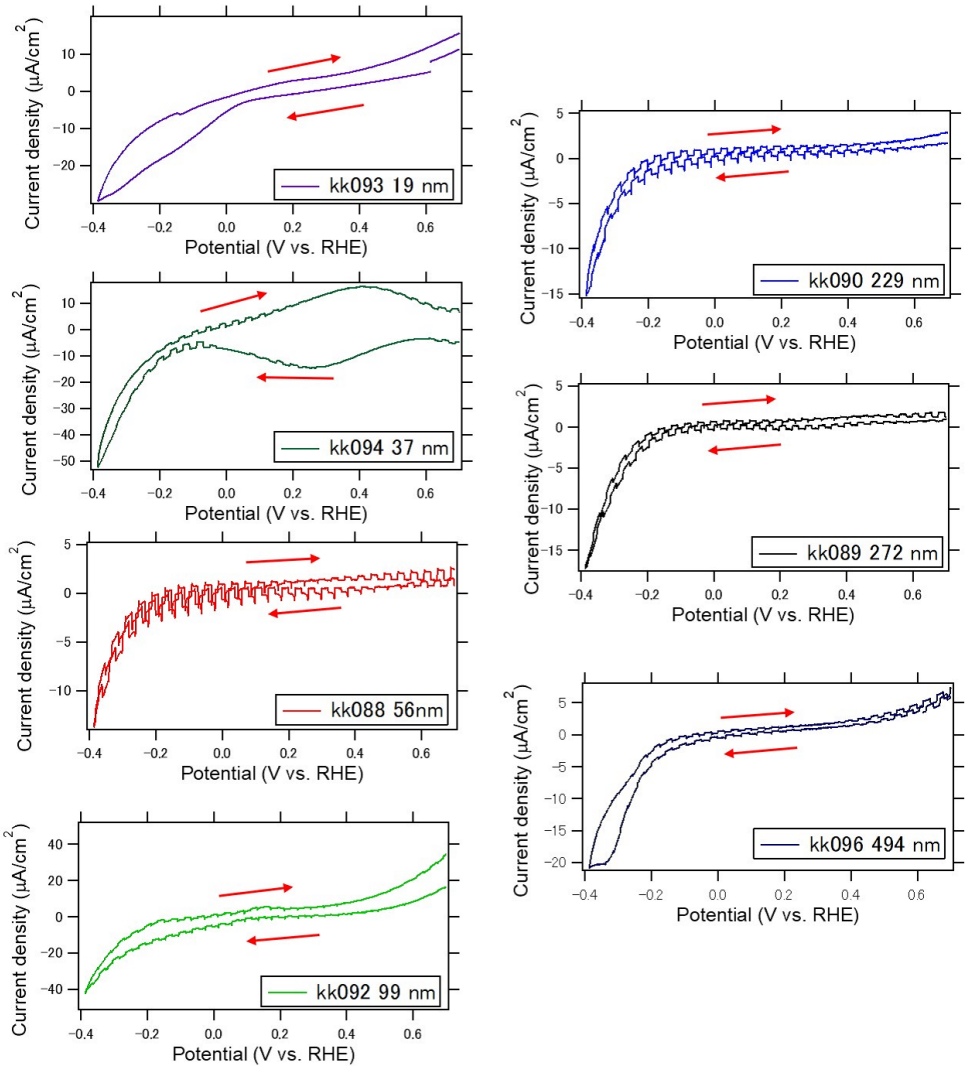

Figure 3.24: Cyclic voltammetry curves of several $BaSnO_3$ samples under illumination with chopped UV light (240-300 nm) from a 100 W Xe lamp.

Fig. 3.24 shows the cyclic voltammetry curves of these samples under illumination with chopped UV light (240 to 300 nm) from a 100 W Xe lamp. The measurements were done in a 0.1 M K_2SO_4 aqueous solution (pH=7) with a Pt counter electrode and a Ag/AgCl reference electrode. The dark current shape and the photoresponse amplitude varies considerably between samples. These differences are probably caused by crystallinity changes due to the large lattice mismatch and SnO_2/BaO composition ratio

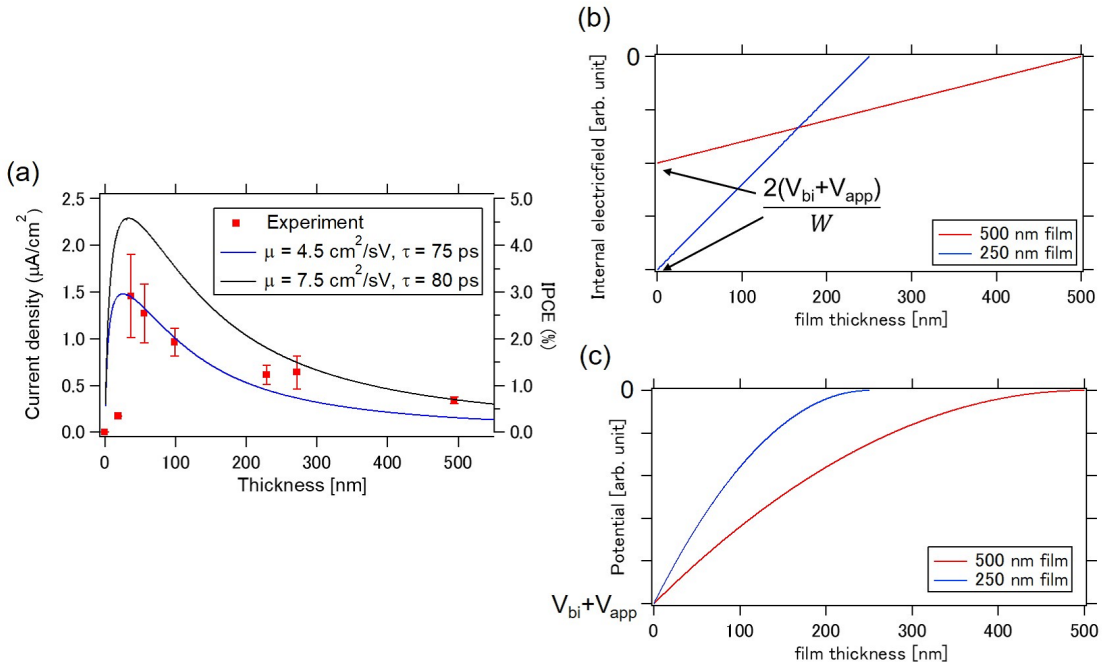

Figure 3.25: (a) Photoinduced current density of $BaSnO_3$ films at -0.1 V vs RHE as a function of film thickness (red dots). Simulation results of IPCE with μ = 4.5 cm^2/sV and τ = 75 ps (blue line), μ = 7.5 cm^2/sV and τ = 80 ps (black line). (b,c) Linear internal electric field and the quadric potential corresponding to the band bending in the case of 250 nm and 500 nm thick films.

changes. In the case of Rh-doped $SrTiO_3$, the dark current shapes were quite similar for film thicknesses between 20 and 300 nm, as shown Fig.3.21(a). Rh-doped $SrTiO_3$ has a good lattice match with Sr_2RuO_4 film and the $SrTiO_3$ substrate, which means that thickness-dependent crystallinity changes are negligible in the Rh-doped $SrTiO_3$ experiments. The photoinduced current density of $BaSnO_3$ films at −0.1 V vs RHE as a function of the film thickness is shown with red dots in Fig. 3.25(a). The thickness of the $BaSnO_3$ thin films clearly affects the photoelectrochemical performance. This thickness dependence can be understood in terms of light absorption and charge transport efficiency: when the film thickness become thicker, the amount of absorbed light is increased but the efficiency of charge transport to the semiconductor surface decreases. The simulation of the incident photon to current efficiency (IPCE) was conducted to estimate the photocarriers lifetime and mobility. Although the photoinduced current density with the 100 W Xe lamp is not perfectly proportional to IPCE, IPCE should show a similar film thickness dependence. A linear internal electric field was assumed in the whole semiconductor thickness in this simulation [57]. Figs. 3.25(b,c) show the

linear internal electric field and quadric potential corresponding band bending in the case of 250 nm and 500 nm thick films. The force acting on a photocarrier at a certain depth depends on the film thickness as shown in Fig. 3.25(b), providing thickness dependence of charge transport efficiency. The incident photon to current efficiency (IPCE) was calculated using the following equations:

$$\mathrm{IPCE}(\%) = (1-R)\beta \int_0^W \alpha \exp(-\alpha x)(1-\frac{x}{W})^{\frac{W}{\mu\tau E}} dx, \tag{3.6}$$

$$E = \frac{V_{\mathrm{bi}} + V_{\mathrm{app}}}{W}, \tag{3.7}$$

$$\beta = \frac{1}{1+\frac{S}{\mu E}}, \tag{3.8}$$

where R is the reflectance of the sample, α is the absorption coefficient, W is the film thickness, β is a collection parameter at the sample surface, μ is the carrier mobility, τ is the carrier lifetime, S is the recombination velocity, V_{bi} is the built-in potential in the space charge region in the semiconductor and V_{app} is the applied bias. The parameter value used in the simulation were: $R = 0.1$, $\alpha = 10^5$ cm^{-1}, $S = 10^7$ cm/s, $V_{\mathrm{bi}} = -0.4$ V and $V_{\mathrm{app}} = -0.1$ V.

The IPCE simulation results are plotted with a blue line for $\mu = 4.5$ cm^2/sV, $\tau = 75$ ps and with a black line for $\mu = 7.5$ cm^2/sV, $\tau = 80$ ps. Although the simple model doesn't allow perfect fitting, a carrier lifetime estimate can be found. The simulation doesn't consider possible thickness-dependent crystallinity changes of the films caused by a large lattice mismatch between the film and the substrate. Thinner films have lower crystallinity, resulting in lower performance as shown by the blue line. Crystallinity improves as the $BaSnO_3$ films become thicker, following the black line. To validate this simulation, The IPCE was measured for 494 nm $BaSnO_3$ sample (kk096) with the monochromator (Bunkoukeiki, BML-10J). Figs. 3.26 (a,b) show the cyclic voltammetry curves of this sample under illumination with chopped light at the wavelength of 300 nm and 350 nm,respectively. The photocurrent value under light illumination at 350 nm was used for IPCE calculation because the photocurrent at -0.1V vs RHE was too small when the wavelength of light less than 300 nm was illuminated due to weak light intensity of the monochromator. The IPCE was calculated as 0.74 % from the current density 0.99 μA/cm^2 and light intensity 0.48 mW/cm^2. Although the illuminated wavelength was different from Xe lamp, this value is in good agreement with the simulation result. This means that the simulation is reasonable. Thus, the electron drift mobility and lifetime of $BaSnO_3$ were estimated to be in the range of $\mu = 4.5$ to 7.5 cm^2/sV and $\tau = 75$ to 80 ps. From these results, it was concluded that the photocarrier mobility of $BaSnO_3$ is much lower than the Hall mobility obtained by La-doping and the lifetime is on the order of picoseconds. This means that high efficiency of photoelectrochemical performance cannot be expected even for $BaSnO_3$, even though the material has a highly dispersive conduction band.

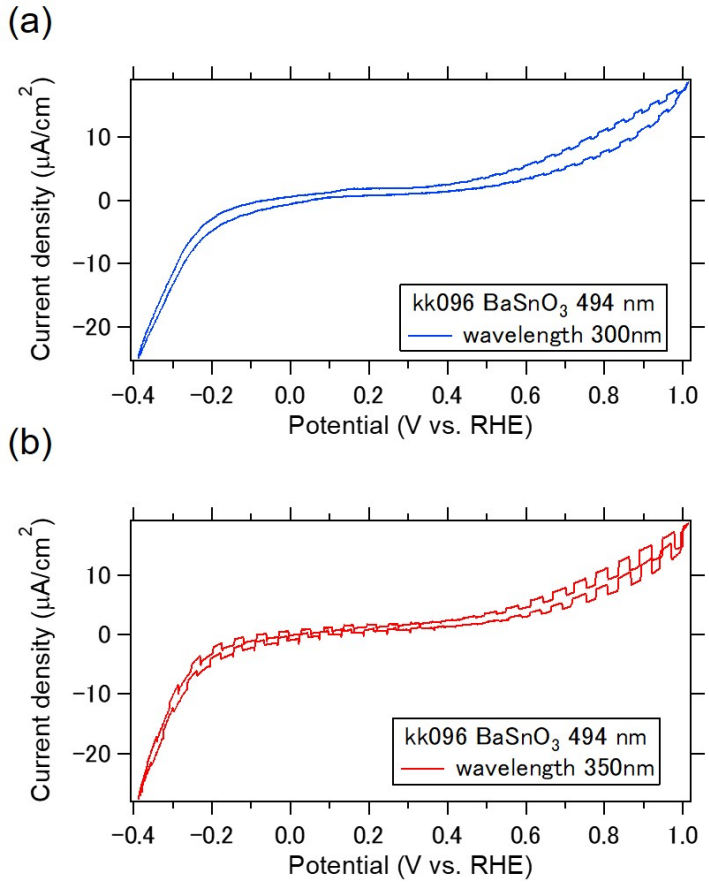

Figure 3.26: The cyclic voltammetry curves of 494 nm $BaSnO_3$ sample under illumination with chopped light at the wavelength of (a) 300 nm and (b) 350 nm..

Chapter 4

Conclusion

4.1 Summary

Solving the energy supply problems in an environmentally acceptable manner requires solutions to two major problems of collecting energy and storing energy. Hydrogen may play an important role in this solution since it is possible clean energy carrier and solar energy can be used to directly produce hydrogen from water either in a photocatalytic or a photoelectrochemical water splitting cell. However, efficient wide-gap semiconductor materials that can be used as light-absorbing photoelectrodes in water splitting cells have not been found so far.

It is therefore quite important to study the physical processes that limit the energy conversion efficiency in semiconductor materials. In particular, the low drift mobility of photoexcited carriers is a factor that severely limits the solar energy harvesting efficiency.

In this work, I analyzed the drift mobility of photoexcited carriers in non-doped $BaSnO_3$ thin films. $BaSnO_3$ can be expected to show high electron drift mobility due to a large dispersion of the conduction band. An attempt was made to measure the drift mobility by the time-of-flight (TOF) technique. The measurement probes the migration of photogenerated charge and thus represents a similar physical system as exists in photoelectrochemical water splitting cells under light illumination.

The optimization of the PLD growth conditions of $BaSnO_3$ thin film to obtain the best crystallinity is discussed in Chapter 3.1. It was concluded that $SrTiO_3$ is a suitable substrate material for the growth of $BaSnO_3$ films with good crystallinity and that the optimal conditions for $BaSnO_3$ film growth are 750 to 800°C and 10 to 50 mTorr oxygen pressure.

The optical absorption properties of $BaSnO_3$ thin films are discussed in Chapter 3.2. $BaSnO_3$ thin films were grown on MgO substrate for optical measurement. This substrate material has a larger optical band gap than $BaSnO_3$, which makes it possible to measure the absorption spectrum of the film. The measurements showed that reason-

able indirect band gap (2.94 eV) and direct band gap (3.48 eV) values can be obtained. The absorption coefficient was measured to determine the depth of the photoexcitation used in the TOF experiments.

The self-made TOF measurement setup is introduced in Chapter 3.3. A test measurement was made with a high-resistivity Si single crystal and it was shown that the simple TOF measurement system works as intended. An attempt was made to measure the drift mobility of $BaSnO_3$ thin films with the TOF measurement system. $BaSnO_3$ thin films were grown for these experiments on 0.5wt% Nb-doped $SrTiO_3$ substrates that are metallic and can be used as a bottom electrode. The electron drift mobility obtained by the TOF method for the $BaSnO_3$ thin films was 6.3×10^{-3} cm^2/sV. However, this value was found to be unreliable due to space charge effects. It was found that it is impossible to measure the real drift mobility of photocarriers in a $BaSnO_3$ thin film with this TOF setup due to heavy trapping and a subnanosecond carrier lifetime. The measurements showed that the diffusion length of photocarriers in the $BaSnO_3$ thin film is much shorter than the film thickness.

The photoelectrochemical performance of $BaSnO_3$ thin films is discussed in Chapter 3.4. The lifetime and mobility of photoexcited carriers in $BaSnO_3$ were estimated by fitting the film thickness dependence of photoelectrochemical activity.
$BaSnO_3/Sr_2RuO_4/SrTiO_3$ heterostructures were used in the photoelectrochemical measurements, where Sr_2RuO_4 was used as a bottom electrode. The measurements indicated that despite the favorable band structure, even in $BaSnO_3$, high-efficiency photoelectrochemical performance was not obtained. The lifetime and drift mobility of photocarriers in $BaSnO_3$ were estimated to be in the range of $\mu = 4.5$ to 7.5 cm^2/sV and $\tau = 75$ to 80 ps by simulation.

4.2 Conclusion

High drift mobility of photocarriers and high efficiency of photoelectrochemical performance cannot be expected even for $BaSnO_3$, even though the material has a highly dispersive conduction band. The long range electron mobility obtained by TOF analysis was 6.3×10^{-3} cm^2/sV. The simulated IPCE was a few percent under UV irradiation. These results are most probably due to heavily trapping that limits the photocarrier trapping lifetime to picosecond order. Accurate measurement of the drift mobility by TOF is impossible if the lifetime is below about 1 ns. A short carrier lifetime also limits the efficiency of photoelectrochemical energy conversion because photocarriers cannot migrate to the semiconductor surface. Although the photocarrier lifetime and drift mobility may improve if films are grown by a different growth technique, such as molecular beam epitaxy, or if homoepitaxial films are used [16, 59], these options would not solve the problem of scaling for practical use.

In general, non-doped oxide materials always have empty trap states due to intrinsic

vacancies or defects. This means that the diffusion length of photocarrier is strongly limited by trapping and the drift mobility of photocarrier is much lower than the Hall mobility obtained by doping an insulating oxide to a metallic state. In conclusion, high-crystallinity material such as Si, where the photocarrier lifetime is much longer than in oxide materials, should be used for solar energy harvesting in conjunction with suitable oxide electrodes for water splitting to produce hydrogen fuel.

References

[1] A. Fujishima and K. Honda, Electrochemical photolysis of water at a semiconductor, *Nature*, **238**, 37, (1972).

[2] R. Konta, et al., Photocatalytic Activities of Noble Metal Ion Doped $SrTiO_3$ under Visible Light Irradiation, *J. Phys. Chem. B*, **108**, 26, 8992, (2004).

[3] R.U.E. 't Lam, L.G.J. de Haart, et al., THE SENSITIZATION OF SrTiO. PHOTOANODES BY DOPING WITH VARIOUS TRANSITION METAL IONS, *Mat. Res. Bull.*, **16**, 1593, (1981).

[4] S. Kawasaki, et al., Epitaxial Rh-doped $SrTiO_3$ thin film photocathode for water splitting under visible light irradiation, *Appl. Phys. Lett.*, **101**, 033910, (2012).

[5] A. Kudo and Y. Miseki, Heterogeneous photocatalyst materials for water splitting, *Chem. Soc. Rev.*, **38**, 253, (2009).

[6] Y. Inoue, Photocatalytic water splitting by RuO2-loaded metal oxides and nitrides with d^0- and d^{10} -related electronic configurations, *Energy Environ. Sci.*, **2**, 364, (2009).

[7] J. Sato, et al., New Photocatalyst Group for Water Decomposition of RuO_2-Loaded p-Block Metal (In, Sn, and Sb) Oxides with d10 Configuration, *J. Phys. Chem.*, **105**, 6061, (2001).

[8] T. Yanagida, et al., Photocatalytic Decomposition of H_2O into H_2 and O_2 over Ga_2O_3 Loaded with NiO, *Chem. Lett.*, **33**, 726, (2004).

[9] J. Sato, et al., Photocatalytic Activity for Water Decomposition of RuO_2-Dispersed Zn_2GeO_4 with d^{10} Configuration, *J. Phys. Chem. B*, **108**, 4369, (2004).

[10] H. J. Kim, et al. Physical properties of transparent perovskite oxides (Ba,La)SnO_3 with high electrical mobility at room temperature, *Phys. Rev. B*, **86**, 165205 (2012).

[11] Q. Liu, et al. Electrical and optical properties of Sb-doped $BaSnO_3$ epitaxial films grown by pulsed laser deposition, *J. Phys. D: Appl. Phys.*, **43**, 455401, 7, (2010).

[12] S. A. Chambers, et al. Band alignment at epitaxial $BaSnO_3/SrTiO_3(001)$ and $BaSnO_3/LaAlO_3(001)$ heterojunctions, *Appl. Phys. Lett.*, **108**, 152104 (2016).

[13] H.Mizoguchi, et al. Probing the Electronic Structures of Ternary Perovskite and Pyrochlore Oxides Containing Sn^{4+} or Sb^{5+}, *Inorg. Chem.*, **43**, 5, 1667 (2004).

[14] H. J. Kim, et al. High Mobility in a Stable Transparent Perovskite Oxide, *Appl. Phys. Express*, **5**, 061102, (2012).

[15] C. A. Niedermeier, Solid phase epitaxial growth of high mobility La:$BaSnO_3$ thin films co-doped with interstitial hydrogen, *Appl. Phys. Lett.*, **108**, 172101 (2016).

[16] S. Raghavan, et al. High-mobility $BaSnO_3$ grown by oxide molecular beam epitaxy, *APL Mater.* **4**, 016106 (2016).

[17] A. V. Sanchela, et al. Thermopower modulation clarification of the intrinsic effective mass in a transparent oxide semiconductor, $BaSnO_3$, *Phys. Rev. Materials*, **1**, 034603 (2017).

[18] E. Moreira, et al., Structural and optoelectronic properties, and infrared spectrum of cubic $BaSnO_3$ from first principles calculations. *J. Appl. Phys.*, **112**, 043703 (2012).

[19] B. Hadjarab, et al., Optical and transport properties of lanthanum-doped stannate $BaSnO_3$. *J. Phys. D: Appl. Phys.*, **40**, 5833 (2007).

[20] J. C. Bean, Silicon/metal silicide heterostructures grown by molecular beam epitaxy, *Appl. Phys. Lett.*, **36**, 741 (1980).

[21] ミック リップマー, パルスレーザー堆積法と表面処理を使った低次元構造の作製とその特性評価, 応用物理, 75, 3, 304, （2006).

[22] W. E. Spear, et al. The Hole Mobility in Selenium, *Proc. Phys. Soc.*, **76**, 826, (1960).

[23] P.J. Sellin, et al. Drift Mobility and Mobility-Lifetime Products in CdTe:Cl Grown by the Travelling Heater Method, *IEEE Trans. Nucl. Sci.*, **52**, 6, (2005).

[24] W. D. Gill, et al. Drift mobilities in amorphous charge-transfer complexes of trinitrofluorenone and poly-n-vinylcarbazole, *J. Appl. Phys.*, **43**, 12, (1972).

[25] M. Kitamura, et al. Time-of-Flight Measurement of Lateral Carrier Mobility in Organic Thin Films, *Jpn. J. Appl. Phys.*, **43**, 4B (2004).

[26] A. Kuwahara, et al. Carrier mobility of organic thin films using lateral electrode structure with optical slits, *Appl. Phys. Lett.*, **89**, 132106, (2006).

[27] W. E. Spear, DRIFT MOBILITY TECHNIQUES FOR THE STUDY OF ELECTRICAL TRANSPORT PROPERTIES IN INSULATING SOLIDS, *J. OF Nno Cryst. Solids*, **1**, 197, (1969).

[28] M. B. Prince, Drift Mobilities in Semiconductors. I. Germanium, *Phys. Rev.*, **92**, 3, (1953).

[29] J. R. Haynes, and W. C. Westphal, The Drift Mobility of Electrons in Silicon, *Phys. Rev.*, **85**, 680, (1952).

[30] R. K. Ahrenkiel, e al. Electron mobility in p-GaAs by time of flight, *Appl. Phys. Lett.*, **51**, 776, (1987).

[31] Z. Galazka, et al. Melt growth and properties of bulk $BaSnO_3$ single crystals, *J. Phys.: Condens. Matter*, **29**, 075701(2017).

[32] J.Park, et al. Photoconductivity of transparent perovskite semiconductor $BaSnO_3$ and $SrTiO_3$ epitaxial thin films, *Appl. Phys. Lett.*, **108**, 092106 (2016).

[33] JCPDS 00-015-0780.

[34] JCPDS 00-005-0634

[35] JCPDS 01-076-5381.

[36] JCPDS 01-074-9387.

[37] J. Shiogai, et al. Improvement of electron mobility in La:BaSnO3 thin films by insertion of an atomically flat insulating (Sr,Ba)SnO_3 buffer layer, *AIP Adv.*, **6**, 065305 (2016).

[38] H. F. Wang, et al. Transparent and conductive oxide films with the perovskite structure: La and Sb doped $BaSnO_3$, *J. Appl. Phys.*, **101**, 106105, (2007).

[39] A. Prakash, et al. Adsorption-controlled growth and the influence of stoichiometry on electronic transport in hybrid molecular beam epitaxy-grown BaSnO3 films, *J. Mater. Chem. C*, **5**, 5730, (2017). *Appl. Phys. Lett.*, **108**, 152104 (2016).

[40] JCPDS 01-074-1349.

[41] JCPDS 00-025-0077.

[42] JCPDS 00-025-1259.

[43] JCPDS 00-004-0673.

[44] J. Tauc, et al. Optical Properties and Electronic Structure of Amorphous Germanium, *Phys. Stat. Sol*. **15**, 627 (1966).

[45] D. E. Aspnes and A. A. Studna, Dielectric functions and optical parameters of Si, Ge, GaP, GaAs, GaSb, InP, InAs, and InSb from 1.5 to 6.0 eV, *Phys. Rev. B*, **27**, 2, (1983).

[46] D. J. Gibbons and A. C. Papadakis, TRANSIENT SPACE-CHARGE PERTURBED CURRENTS IN ORTHORHOMBIC SULPHUR, *J. Phys. Chem. Solids*, **29**, 115, (1968).

[47] 舟橋正浩, Time-of-Flight 法によるキャリア移動度測定, EKISHO, 17, 1, 55, (2013).

[48] S. S. Li and R. Thurber, THE DOPANT DENSITY AND TEMPERATURE DEPENDENCE OF ELECTRON MOBILITY AND RESISTIVITY IN n-TYPE SILICON, *Solid. State Electron.*, **20**, 609, (1977).

[49] JCPDS 00-005-0626.

[50] K. Terai, et al. In-plane lattice constant tuning of an oxide substrate with $Ba_{1-x}Sr_xTiO_3$ and $BaTiO_3$ buffer layers, *Appl. Phys. Lett.*, **80**, 23, 10, (2002).

[51] G. Pfister, Pressure-Dependent Electronic Transport in Amorphous As_2Se_3, *Phys. Rev. Lett.*, **33**, 25, (1974).

[52] H. Scher, Anomalous transit-time dispersion in amorphous solids, *Phys. Rev. B*, **12**, 6, (1975).

[53] W. E. Spear, The Hole Mobility in Selenium, *Proc. Phys. Soc.*, **76**, 826, (1960).

[54] W. E. Spear, Transit Time Measurement of Charge Carriers in Amorphous Selenium Films, *Proc. Phys. Soc. B*, **70**, 669, (1957).

[55] H. T. Grahn, et al. Picosecond optical Time-of-Flight Studies of Carrier Transport in a-Si:H-a-SiN_x:H Multilayers, *Phys. Rev. Let.*, **59**, 10, (1987).

[56] S. Kawasaki, Doctoral thesis, (2016).

[57] A. E. Delahoy, et al. *27th European Photovoltaic Solar Energy Conference and Exhibition, Frankfurt, Germany*, 2837, (2012).

[58] JCPDS 00-043-0217.

[59] W. J. Lee, et al. Enhanced electron mobility in epitaxial (Ba,La)SnO_3 films on $BaSnO_3$(001) substrates, *Appl. Phys. Lett.*, **108**, 082105 (2016).

Acknowledgment

I would like to show my greatest appreciation to Prof. Mikk Lippmaa for his excellent guidance, advice and supports in these two years. He gave me an opportunity to learn oxide thin films, semiconductors and photocatalytic water splitting. His kind lecture is very informative for me and I have learned a lot of things besides my research topic. When I had a trouble with experiment process, he always gave me useful advice and gave me a hand on handling technical problems. I have learned a lot of things from him and this experience will be invaluable in my life.

I am also deeply grateful to Dr. Ryota Takahashi. He taught me how to use equipment and gave me valuable advice about my research. He always took care of students and encouraged me when my experiment didn't go well. I would like to thank laboratory member. Mr. Xiuyi Hou, Mr. Naoyuki Osawa and Ms. Jiyeon Lee taught me the basics of thin film fabrication and how to use equipment to proceed my experiment. Mr. Yoshihisa Hosokawa gave me advice about the growth condition of Sr_2RuO_4 and photoelectrochemical measurement. Mr. Kodai Ogawa is studying interesting research topic. It made me interested. Ms. Junko Kawamura is very kind to students and always help me for administrative work. And I would like to thank everyone for making me fun in my daily life. I could have fulfilling days in lippmaa laboratory thanks to everyone for these two years.

Finally, I would like to offer my special thanks to my family for their great support and encouragement in my life.

January 2018

Katsuya Kihara